Sonar Observations of Langmuir Circulation and Estimation of Dispersion of Floating Particles

S. A. THORPE, M. S. CURE,* AND A. GRAHAM

Department of Oceanography, University of Southampton, Southampton, United Kingdom

A. J. HALL

Institute of Oceanographic Sciences Deacon Laboratory, Wormley, Godalming, Surrey, United Kingdom

(Manuscript received 21 June 1993, in final form 15 February 1994)

ABSTRACT

Observations are described of Langmuir circulation obtained using upward-pointing bottom-mounted sonars, and a methodology to use the data to estimate the dispersion of floating particles is suggested. Observations of linear bands of acoustic scatterers separated by 2–20 m and detected using side-scan sonar in Loch Ness, Scotland, and in the southern North Sea are ascribed to subsurface bubbles in the convergence zones produced by Langmuir circulation. Data from the two observation sites are compared. The sonar is able to monitor the variability of the patterns over many hours. When the currents are sufficiently small, as in Loch Ness, individual bubble clouds produced by breaking waves remain in the beam long enough for their speed to be resolved, and the rate of convergence into the bands can be estimated. It increases linearly with wind speed. The acoustic data and direct measurements using current meters are used to derive estimates of the response time of bubble bands to changes in wind, and their mean separation, length, and persistence time. The bands in Loch Ness are shorter, but persist longer, than those in similar wind conditions in the relatively shallow and well-mixed North Sea. It is suggested that these differences may be ascribed to the presence of turbulence generated by the shear stress of the strong tidal currents on the seabed in the North Sea, a factor absent in Loch Ness. Models are devised to simulate the dispersion of plumes of floating particles released from a fixed position in a field of Langmuir circulation advected by tidal currents, using the sonar data. The estimates of diffusivities show an increase with wind speed, but are sensitive to the choice of some underdetermined parameters. The resulting estimates of lateral dispersion of floating particles overlap the range of those of Faller and Auer.

1. Introduction

Moored or towed, upward-pointing, high-frequency side-scan sonars have now been used for some 10 years to obtain graphic insight and quantitative information about a variety of processes that operate at, or close to, the sea surface. The sonars used, typically emitting short 10–30-cm-long pulses at 50–250 kHz, are able to detect the injection into the water of clouds of microbubbles by breaking wind waves, and subsequently to follow the clouds' motion in response to mean flows and turbulence at scales exceeding those of the clouds. The bubbles have small rise speeds (50-μm-radius bubbles rise at about 5 mm s^{-1}), usually much less than the mean flows that advect them. Winds greater than 3 m s^{-1} are generally sufficient to produce detectable bubble clouds. Although the vertical scale of the clouds increases with wind speed, clouds reaching to 10-m depth in wind speeds of 10 m s^{-1} (Thorpe 1982; Crawford and Farmer 1987), the acoustic scattering falls off rapidly with depth below the surface with an e-folding scale of 0.6–2.4 m (Thorpe 1986), so that much of the scattering comes from close to the sea surface. The clouds have lifetimes of several minutes before the bubbles dissolve, rise to the surface, or can no longer be detected by the sonar. During this time they are advected by near-surface currents. Estimates of the current speed relative to the sonar can be inferred from the observed rate of change of range of individual bubble clouds from the sonar, estimated from the time between transmitted and returned pulses of sound and its known speed in water (Thorpe and Hall 1983).

Several processes that affect the dynamics of the upper-ocean boundary layer have been subject to special, but by no means exhaustive, sonar study, for example, the frequency of breaking waves (Thorpe and Humphries 1980; Thorpe 1993) and their spatial distribution, for instance, in relation to the phase or position

* Current affiliation: Department of Oceanography, Martin Ryan Institute, University College of Galway, Galway, Ireland.

Corresponding author address: Dr. S. A. Thorpe, Department of Oceanography, University of Southampton, Southampton, SO9 5NH United Kingdom.

of internal waves (Thorpe et al. 1987). Studies of the approach of waves to shore illustrate, for example, the occasional dominance and regularity of wave groups (Smith 1993; Thorpe and Hall 1983) and the presence of Langmuir circulation in shallow water. The information from deep water has been used to infer the rates of transfer of gases from the atmosphere to the ocean and the consequent generation of supersaturated conditions in the water column (Woolf and Thorpe 1991; Farmer et al. 1993).

Here we describe how the sonar can provide a vivid demonstration and quantitative measure of the presence of Langmuir circulation and explain how the acquired data may be used in the study of the horizontal dispersion of buoyant particles. Such dispersion is caused by the motion of particles into, and within, the regions of surface convergence associated with Langmuir circulation and, in particular, with the redistribution of the material as the local circulation pattern breaks up and forms afresh in both space and time. The sonar data have been incorporated into a numerical simulation of motion to provide quantitative estimates of dispersion of floating particles at the dominant scale of the circulation. [A preliminary account of this technique for one-dimensional dispersion is given by Thorpe and Curé (1994)].

The general effects of Langmuir circulation on the dispersion of floating material are introduced in section 2. Data collected in preliminary experiments made in a freshwater lake, Loch Ness in Scotland, and in later experiments in the southern North Sea are described in section 3. The method used to determine the dispersion of floating particles is described in section 4a, and the selected ranges of parameters used are discussed in section 4b. In section 4c, estimates are derived that illustrate the potential use of sonar in dispersion measurements in the North Sea, but a detailed comparison with rates of dispersion measured at sea at the same time and place as our sonar studies is reserved until a later publication. A main conclusion (section 5) reached after a comparison of the Loch Ness and North Sea datasets is that the turbulence generated by the shear stress of the tidal currents on the seabed in shallow seas plays a dual role by directly promoting dispersion and by affecting surface-generated turbulence, to which the main contributor at the scales of interest is Langmuir circulation.

2. Langmuir circulation and dispersion

The effect of Langmuir circulation on the dispersion of floating material led to its discovery by Langmuir (1938). It produces the wind rows or parallel lines of foam and other floating material that appear on the surface of the sea and lakes in moderate and strong winds, and these provide evidence of the presence of the underlying circulation on the sea surface. Langmuir described the pattern of parallel vortices of alternating sign with axes aligned roughly downwind producing alternate zones of convergence and divergence at the surface, downward flows beneath convergence, and upward flows below divergence.

Theoretical and laboratory studies reviewed by Pollard (1977) and Leibovich (1983) point to a combination of waves and drift currents as being essential contributors in providing a vortex force to drive the circulation. Observations at sea (e.g., Smith et al. 1987; Weller and Price 1988; Smith 1992) or in lakes (Kenney 1979) show that the vortices are typically 5–200 m apart and lie approximately parallel to the wind direction. Subsurface bubbles are carried into the region below wind rows where they accumulate, partly as a result of their being trapped in recirculating zones by rising against the descending currents in the Langmuir cells. This accumulation creates subsurface bands of bubble clouds beneath the wind rows (Thorpe 1984), which can be detected by side-scan sonar (Thorpe and Hall 1983; Zedel and Farmer 1991; Osborn et al. 1993; Farmer et al. 1993). In productive regions—for example, near fronts—microorganisms (notably those containing gas vacuoles and being buoyant) may be concentrated in a similar way. Langmuir circulation therefore plays a central role in 5–200-m-scale crosswind dispersion, carrying floating particles across wind into convergence regions but then impeding their further spreading until such times as the locally entrapping circulation breaks up, perhaps when one Langmuir cell merges with its neighbor, when the particles may again be transferred across wind to adjacent wind rows, a mechanism first described by Csanady (1973) and later discussed by Faller and Auer (1988) and Thorpe (1992). Dispersion of neutrally buoyant material or soluble substances are not considered in this paper. Unlike floating particles, they are not concentrated by the circulation and their dispersion will be affected by the rate of circulation of water within a cell and exchange from one Langmuir cell to its neighbor by turbulence at a scale small compared to that of the cells, as well as by the local circulation breakdown mechanism just described.

Several timescales are important in the process of dispersion of buoyant particles, and further observational evidence that relates to these is presented in section 3. Symbols used to denote periods of time are listed in Table 1. There is first the mean time t_1 taken for particles to be transported in the circulation pattern from a fixed source at the surface to the convergence zones, the wind rows, where they congregate. This is determined primarily by the mean crosswind separation between wind rows, l_s, and the speed u of the convergent motion induced by the circulation. Typical scales of 10 m and 5 cm s^{-1}, respectively, give $t_1 = l_s/4u = 50$ s. The value of t_1 is of importance since it represents a measure of the time a water particle remains at the free surface before being subducted at the flow-separation line where there is convergence be-

TABLE 1. Symbols used to denote periods of time and place in text of first reference.

t_s	the period for which individual bands are detected by the sonar (section 3a)
$\bar{t}_s$	the average value of t_s (section 3a)
$\langle t_s \rangle_i$	the average of t_s over an ensemble of i features (section 3b)
t_0	the time of release of particles (section 3b)
t_1	the mean time for floating particles to reach a wind row (section 2)
t_2	the mean period for which floating particles remain in a wind row (section 2)
t_3	the time for wind rows to be formed or re-formed after a change in wind (section 2)
t_4	the time taken for a Langmuir cell to be advected past a fixed position by the mean flow (section 2)
T_c	the characteristic timescale for Langmuir circulation used by Faller and Auer (1988), estimated as mean wind row separation divided by 0.03 m s^{-1} (section 2)
T_p	specified feature lifetime (section 4a)
T_s	the mean plus one standard deviation of t_s (section 3a)
τ	the mean lifetime of a wind row (section 2)
Δt	maximum dispersion time (section 3b)

tween neighboring Langmuir cells. It therefore represents a replacement timescale for the surface water, and may be important as a factor in air–sea heat exchange, or in determining the exposure of phytoplankton to light. [Other, shorter, replacement times may affect the air–sea transfer of gases, e.g., Brtko and Kabel (1978); Brumley and Jirka (1988)].

A second timescale is the average time for which particles subsequently remain trapped in the wind row after arrival. This is determined by the "lifetime" of Langmuir cells, τ, defined as the period of time that cells persist before disintegrating or amalgamating with others. It was identified by Csanady (1973, 1974) as providing the essential timescale that determines the rate of lateral diffusion; the lateral eddy-diffusion coefficient was determined simply from

$$K = \frac{l_s^2}{\tau}. \tag{1}$$

The scales l_s and τ are key values in determining the lateral diffusion produced by Langmuir circulation. Faller and Auer (1988) reviewed the estimates of τ and devised a model in which wind rows wander or meander, predicting that

$$K = 0.5\left(\frac{u}{k^3 T_c}\right)^{1/2}, \tag{2}$$

where T_c is a characteristic timescale for the Langmuir circulation, taken to be equal to $l_s/(0.03\ \text{m s}^{-1})$, and k is the wavenumber of the circulation, $k = 2\pi/l_s$, so giving

$$K = 5.5 \times 10^{-3} u^{1/2} l_s, \tag{3}$$

where SI units are used to measure K, l_s, and u. The formula will be compared with our numerical estimates in section 4c.

From earlier observations Thorpe (1992) estimated that τ is about 10–30 min, so that $\tau > t_1$, a condition necessary for substantial accumulation of floating material in a wind row before its disintegration, and hence a condition for wind rows to form and be made visible. It is known, however, that the downwind motion is greater in the wind rows than between them (Kenney 1979; Weller and Price 1988), so that patches of floating material extending across wind will be stretched in the downwind direction. Although observational evidence is lacking, buoyant particles may therefore pass along the region of convergence producing the wind row and, on reaching its end, be released after some time t_2. This provides a second "trapping time" estimate. Wind rows of 50–100-m length with downwind particle flows of 5 cm s^{-1} greater than the mean downwind speed of the convergence pattern would give $t_2 \approx$ 1000–2000 s, so that $t_2 \approx \tau$. The fraction of time particles spend in wind rows is one parameter that provides a measure of their effect on dispersion (see section 4b). Another timescale is the time t_3 for the formation of wind rows following the onset of wind, or for their re-formation after changes in wind speed or direction. This is estimated as 2–30 min (see, e.g., Leibovich 1983; Faller and Auer 1988), a time that may be related to τ (Thorpe 1992). It is much smaller than the timescale of synoptic variability of the forcing wind field, and indicates the prevalence and persistence of Langmuir circulation, except perhaps in conditions of highly variable wind. When buoyant particles or material are released continuously from a fixed source, the pattern of circulation (approximately aligned with the wind) may be advected by, say, a tidal current past the position from which material is released (Thorpe 1994). The crossing time for each cell, t_4, depends upon its length scale and the component of advective current normal to the wind row direction. The magnitude and relative size of these different timescales has an effect on dispersion caused by Langmuir circulation, and this is discussed in the following sections.

3. Sonar observations

a. *Measurements in Loch Ness, Scotland*

1) THE SITE AND SONOGRAPHS

Preliminary and, as it was subsequently found, very instructive observations were made in Loch Ness. Loch Ness is a freshwater lake, some 34 km in length, 1 km wide, with an average depth of 150 m. The sides are steep, sloping at some 40° to the horizontal at the site of the observations, which is 22 km from the southwest end. The loch is aligned in the direction of the dominant southwesterly winds, which tend to be channeled by the surrounding hillsides to blow along the long axis

of the loch. General descriptions of the dynamics of the lake are given by Wedderburn (1907), Wedderburn and Watson (1909), and Thorpe (1977, 1988). Currents are generally small, less than 20 cm s^{-1}, and wind rows are often visible (Thorpe and Hall 1982).

A 90-kHz sonar was positioned on the northwest side of the loch at a depth of 40 m, directed upward at an angle of 20° and across loch into deeper water, producing a beam 2° wide in the horizontal (or about 7 m at 200-m range) and 46° wide in the vertical (angles measured to the −3-dB points). The pulse repetition rate was varied between 1.5 and 4 Hz and the pulse length was 0.1 ms, giving range resolution of about 15 cm. Observations were made during a period in the autumn when the seasonal thermocline depth was 10–30 m, and in unstratified periods in February–March.

We have chosen for analysis periods when the wind was directed along the loch, when the surface winds are therefore less gusty, and when the surface currents and winds are roughly aligned. Figure 1a is a sonograph typical of those obtained in wind of 8 m s^{-1}. It shows dark regions of high bubble target strength associated with the near-surface convergence regions produced by Langmuir circulation (Thorpe 1984). The mean current 195 m along the sonar beam measured by a Savonius rotor at 4.5-m depth and deployed on a yo-yo mooring (Thorpe 1977) was low—0.8 cm s^{-1}. The sonograph shows streaks of bubble clouds (e.g., at *A*) converging into the longer-lived bands marking the Langmuir pattern. A total of 40 such periods have been processed to give their convergence speeds. The average speed of convergence into the bands is shown in Fig. 2 as a function of wind speed. Each estimate represents an average of about 100 measurements for 1–2-h periods of steady winds. The graph shows an increase of convergence speed u with wind speed W_{10} with a least-squares fit given by

$$u\,(\mathrm{m\ s^{-1}}) = 3.42 \times 10^{-3} W_{10}\,(\mathrm{m\ s^{-1}}) + 2.7 \times 10^{-3}. \quad (4)$$

No significant difference is found between stratified and nonstratified conditions.

2) The skeleton plots

The digital records have been processed to reduce the sonographs to maps of surface convergence marked by the linear bubble clouds, or "skeleton" plots. [The processing, and the use of these plots in the subsequent representation of one-dimensional dispersion, is described by Thorpe and Curé (1994).] Figure 1b is the skeleton plot of Fig. 1a. Some features are present that are aligned suggesting that they may belong to a single continuous physical feature that is not fully delineated by the sound-scattering bubbles, perhaps because their supply from breaking waves is insufficient at some times and positions to provide acoustic targets. If this is so, the persistence of such physical features will be underestimated from the skeleton plots and the distance between neighboring features will be overestimated. (Similar problems occur in estimating the scales of Langmuir circulation from wind rows.) We have no certain way to establish the continuity, or otherwise, of the features, and have therefore made a pragmatic decision to analyze the data as it is (or with some assumptions that are explained later) in a way that other observers could repeat. We appreciate that this provides a more complete description of the distribution of the acoustic scatterers rather than that of the convergence regions in Langmuir circulation, but it does provide bounds for the Langmuir circulation and a basis for comparison both with existing observations of Langmuir circulation and also between different observation sites in similar conditions of wind forcing (section 5). It is important to note that, in the dispersion model described in section 4, short breaks occurring in linear features will not result in much additional dispersion since particles released at the end of one skeleton line in what should perhaps be a continuous feature will not diverge far before being retrapped by the next, disconnected part of the feature.

Isolated bubble clouds, probably recently created by breaking waves, appear in the sonographs. These are not part of a convergence pattern, nor are they regions into which floating particles released into the water nearby would move. We have chosen (see caption of Fig. 1b) to remove them simply by neglecting features that persist for less than 60 s. This provides a further limit to the scales of features identified by the skeleton plots as contributing to dispersion.

The mean distance between neighboring skeleton lines measured along the sonar beam, and therefore approximately normal to the wind direction, l_s, is plotted against wind speed W_{10} in Fig. 3. A best-fit linear regression is given by

$$l_s\,(\mathrm{m}) = 0.47 W_{10}\,(\mathrm{m\ s^{-1}}) + 9.87. \quad (5)$$

The points are scattered but fall within the error bars calculated by producing skeleton plots with extreme values of the recognition threshold (see figure caption). No difference is found between stratified and nonstratified conditions, nor is any significant relationship found between l_s and the wavelength of surface waves estimated from the dominant wave period. The "characteristic" times T_c of Faller and Auer [1988; see Eq. (2)] estimated to be equal to $l_s/(0.03\ \mathrm{m\ s^{-1}})$, range from 376 s in winds of 3 m s^{-1} to 721 s in winds of 25 m s^{-1}.

Equations (4) and (5) together provide an estimate, $l_s/4u$, of the timescale t_1 for particles to reach a bubble band. Values range from 200 s at W_{10} = 4 m s^{-1} to 60 s at W_{10} = 22 m s^{-1}.

3) The length and lifetime of the bands

We now wish to investigate the spatial information that might be derived from the temporal measurements

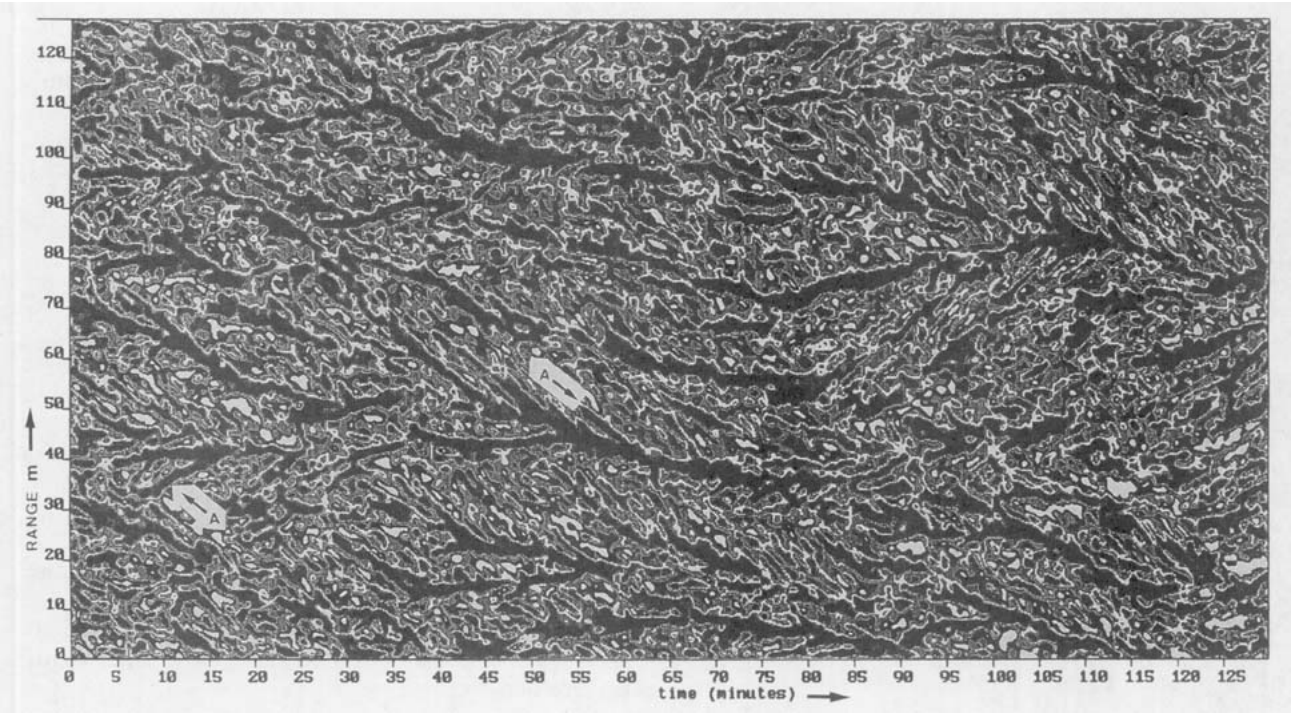

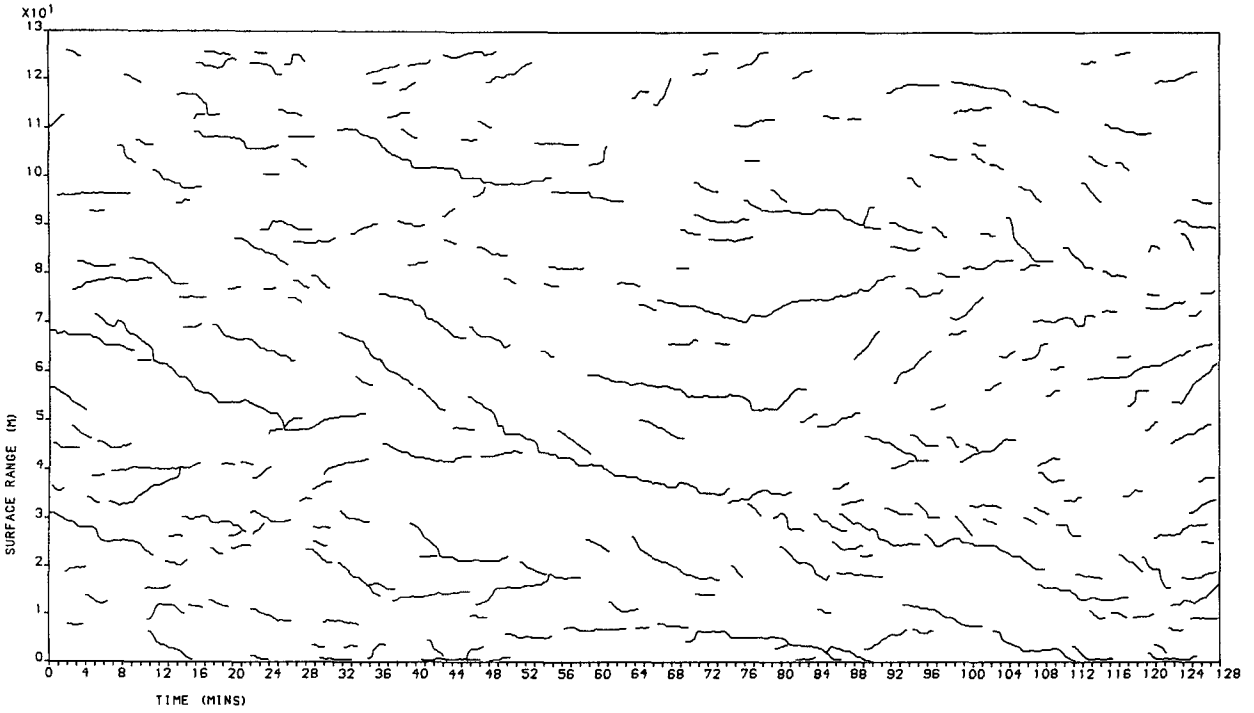

FIG. 1. (a) A sonograph, range along the water surface versus time, typical of the low current advection speeds in Loch Ness. The dark areas are those of greatest scattering. Advection speed 0.8 cm s^{-1}, W_{10} = 8 m s^{-1}. The point of zero range is 100 m from the edge of the loch and 50 m away from the sonar. The sonar beam points directly away from shore. The sonograph has been produced by averaging pulses produced at 2.5 Hz over 8-s periods. (b) The "skeleton" of the sonograph (a). A threshold of 15% of the image with the highest backscatter has been set, reduced to linear form, and "pruned" to remove lines or branches that do not persist for more than 60 s. The threshold intensity is chosen so that 15% of the image area is used as a basis for the production of the skeleton lines. In practice a threshold of 10%–20% is found to be sufficiently low that the band shapes thus derived are of thickness less than half their mean spacing from one another.

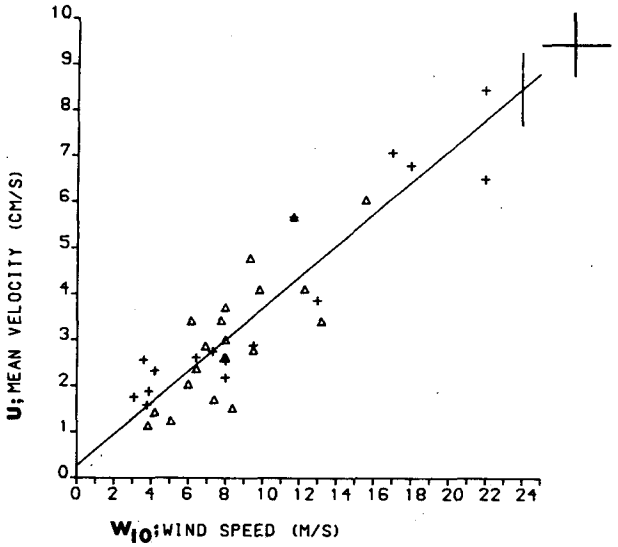

FIG. 2. The average convergence speed into the bubble bands versus W_{10}, obtained from the average of the speeds measured on the two sides of a band. Points are the following: crosses, February–March period; triangles, autumn period. The bars represent the statistical error.

in the fixed sonar beam. To do this we construct a simplified model in which bands of bubble clouds of length L are aligned in a direction (approximately parallel to the wind) at an angle α to the sonar beam, and are carried by a mean uniform current of speed V in direction β relative to the beam (Fig. 4). We suppose that the bands all have the same length L and lifetime τ after which they disintegrate. This important assumption, to which we shall return in section 5, implies that we shall be considering and comparing measurements in similar forcing conditions; in particular, that wind and wave conditions in which the bands are to be compared are similar, and that τ and L are determined primarily by wind speed but not by the strength of the advecting current. The component of flow that carries a band across the beam has speed $V\sin\beta$, and it is this, and the length of the band normal to the beam, $L\sin\alpha$, which determine the crossing time, supposing of course that the band does not disintegrate (and, in this simple model, "vanish") beforehand. We therefore reduce the problem of determining the mean time $\bar{t}_s$ for which bands are "visible" by considering bands of length $L_1 = L\sin\alpha$ being advected normal to the beam at speed $V_1 = V\sin\beta$.

Let x be the distance measured upstream to the leading edge of a band at the instant of its formation. Bands decay before reaching the beam if $x > V_1\tau$. If $x < -L_1$, no part of the band will be "seen." For bands to be seen we need $-L_1 < x < V_1\tau$. Then

(a) if $x = 0$, a band is visible for time $t_s = \min(\tau, L_1/V_1)$;

(b) if $0 < x < V_1\tau$, decay has occurred for a time x/V_1 before the band arrives and so it disintegrates at time $(\tau - x/V_1)$ after arriving. If this exceeds the time for the band to pass with no disintegration, L_1/V_1, then the "observed" time $t_s = L_1/V_1$. If, however, this is less than L_1/V_1, then $t_s = \tau - x/V_1$. These conditions can be written $t_s = L_1/V_1$ if $0 < x < V_1\tau - L_1$; $t_s = \tau - x/V_1$ if $V_1\tau - L < x < V_1\tau$;

(c) if $-L_1 < x < 0$, a similar argument leads to the following conclusions for $x < 0$: $t_s = \tau$ if $0 > x > \tau V_1 - L_1$, and $t_s = (L_1 + x)/V_1$ if $x < \tau V_1 - L_1$.

We can now find the average value

$$\bar{t}_s = \frac{\int_{-L}^{V_\tau} t_s dx}{\int_{-L}^{V_\tau} dx}$$

by integration over the ranges of x. The average value is $\tau(1 + V_1\tau/L_1)^{-1}$.

The mean time for which the bubble bands of length L can be detected as they pass through the sonar beam is therefore

$$\bar{t}_s = \frac{\tau L\sin\alpha}{L\sin\alpha + V\tau\sin\beta}. \qquad (6)$$

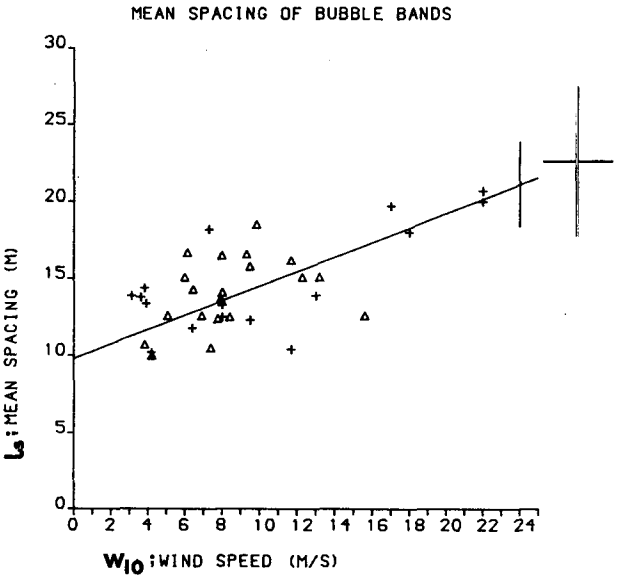

FIG. 3. The frequency distribution of the separation of bands, l_s, derived from the distance in range of neighboring bands in the "skeleton" plots (e.g., Fig. 1b, which has a mean separation of 13.8 m) versus W_{10}. Points are the following: crosses, February–March; triangles, autumn. Values of l_s are much less than the length of the sonar beam and are therefore little affected by its finite length. The error estimates for the mean value of l_s have been derived by varying the threshold level (see Fig. 1b) from 10%, which misses many of the features evident in the sonograph, to 20%, which causes features to merge together. The isolated vertical line has a length twice the standard deviation of points from their linear regression line.

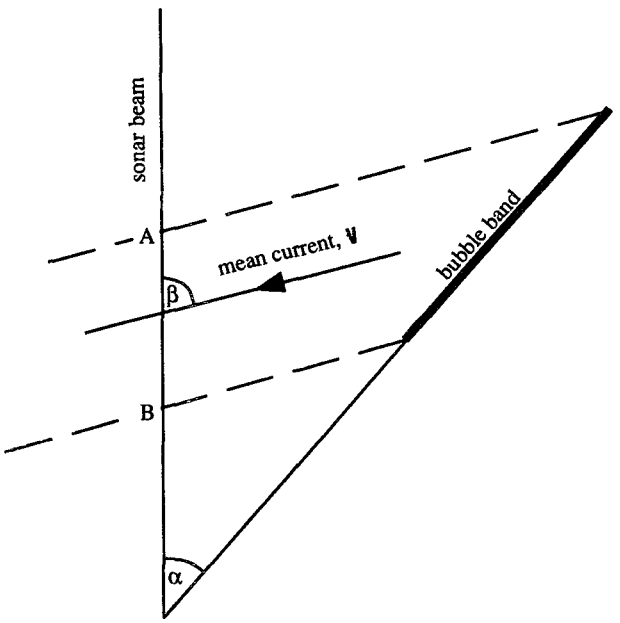

FIG. 4. The advection of a bubble band through a sonar beam by a mean current V. The angles α and β are the angles of the band and the mean flow to the sonar beam, respectively.

If the lifetime of the bands is very large, $\bar{t}_s \approx L \sin\alpha / V \sin\beta$, which is the time for the advection of a band of length $L \sin\alpha$ (the projection of L on a line normal to the beam) through the beam at a speed equal to the component of V normal to the beam. If α or τ tend to zero, so does t_s as expected; bands parallel to the beam or which do not persist in time will not remain to be detected by the narrow sonar beam for any finite time. As V becomes small, the period of detection approaches the lifetime of the bubble band. Advection changes the appearance of the bands in the sonograph record, reducing the period for which they are visible and altering the apparent length of the band in the beam direction (i.e., the length AB in Fig. 4) equal to $L \cos\alpha(1 - \tan\alpha/\tan\beta)$. We may therefore expect the sonographs to show different patterns in conditions of low or high advection even when the geometry is similar. In general the importance of advection is given by the ratio of the terms in the denominator of (6), $V \sin\beta / U \sin\alpha$, where $U = L/\tau$ is a velocity scale which, based on the scales $L \approx$ 50–100 m and $\tau \approx$ 10–30 min (section 2), we expect to be about 10 cm s^{-1}. Much greater flows may (depending on α and β) significantly reduce the time for which bands are visible. In much smaller currents, $\bar{t}_s \approx \tau$.

In reality, bands are present with a range of length scales. If we suppose, as a working hypothesis, that the lifetime of the bands is proportional to their length, so that longer bands persist for longer times, it then follows from integration of (6) over the band-length distribution that the average detection time and the mean lifetime of the bands are still related by an equation of the form of (6), but with $\bar{t}_s$ and τ replaced by their values averaged over the band lengths, provided that the band advection speeds are not dependent on their scale. In general, however, the average detection time may depend on the band-length distribution, and derivation of the subsequent estimates will be correspondingly biased.

The finite length of the sonar beam will effect the estimates of L when the beam length is short compared to AB (Fig. 4). However, in the observations reported here, the correction is small since both α and β are fairly close to 90°. An example of the effect of mean flow on the appearance of the bands in the sonograph is provided in Fig. 5. The sonograph [panel (a)] shows evidence of convergence at a front (AA), which developed in conditions of southwesterly winds and persisted for 16 h. At ranges beyond those of the front the mean current at 4.5-m depth was about 1 cm s^{-1} in the wind direction. Here, as shown in the skeleton plot [panel (b)], bands are much longer than those at smaller ranges where the current was greater, 9 cm s^{-1}, and directed against the wind. [Flows counter to the wind are associated with the circulation of the loch (see Thorpe 1977).]

Figure 6 shows the frequency distribution of t_s for the period shown in Fig. 1 and determined from the skeleton plot. It shows high positive skewness. So as to provide an estimate of the lifetime τ of the bands, we have chosen to use the available current measurements at 4.5 m and to characterize the value of $\bar{t}_s$ by the average measured from the skeleton plots, plus one standard deviation, T_s. This is an arbitrary, but quantified, choice that helped account for the low values attributable to the fragmented nature of the skeleton lines in what appear to be continuous convergence zones (see section 3a). This value, describing the period for which bubble bands are "visible" in the sonar beam, is marked in Fig. 6. Figure 7a shows the reciprocal of T_s plotted against the mean current V averaged over periods of 1 h. A linear relationship is predicted by (6) when the forcing conditions, here principally the wind speeds, are similar. Dividing the graph into points with winds greater than, or less than, 8 m s^{-1}, and fitting straight lines to each, we find least-squares estimates of τ = 33 min, L = 51 m for mean winds of 9.4 ± 0.8 m s^{-1}, and τ = 13 min, L = 59 m for mean winds of 6.2 ± 1.6 m s^{-1}. The estimated errors, determined by selecting extreme values of the thresholds used to derive the "skeletons" (see caption to Fig. 3 for details), are ±8 min in τ, and ±9 m in L. The error estimates, here and later, represent one standard deviation from the mean. The values of τ greatly exceed Faller and Auer's estimates of the "characteristic" timescale T_c. The estimates for L, together with the data of Fig. 3, imply that the aspect ratio of the bubble bands, their mean length divided by their mean spacing, ranges from approximately 4.6 at W_{10} = 6.2 m s^{-1} to 3.5 at W_{10} = 9.4 m s^{-1}. These estimates are much smaller than those

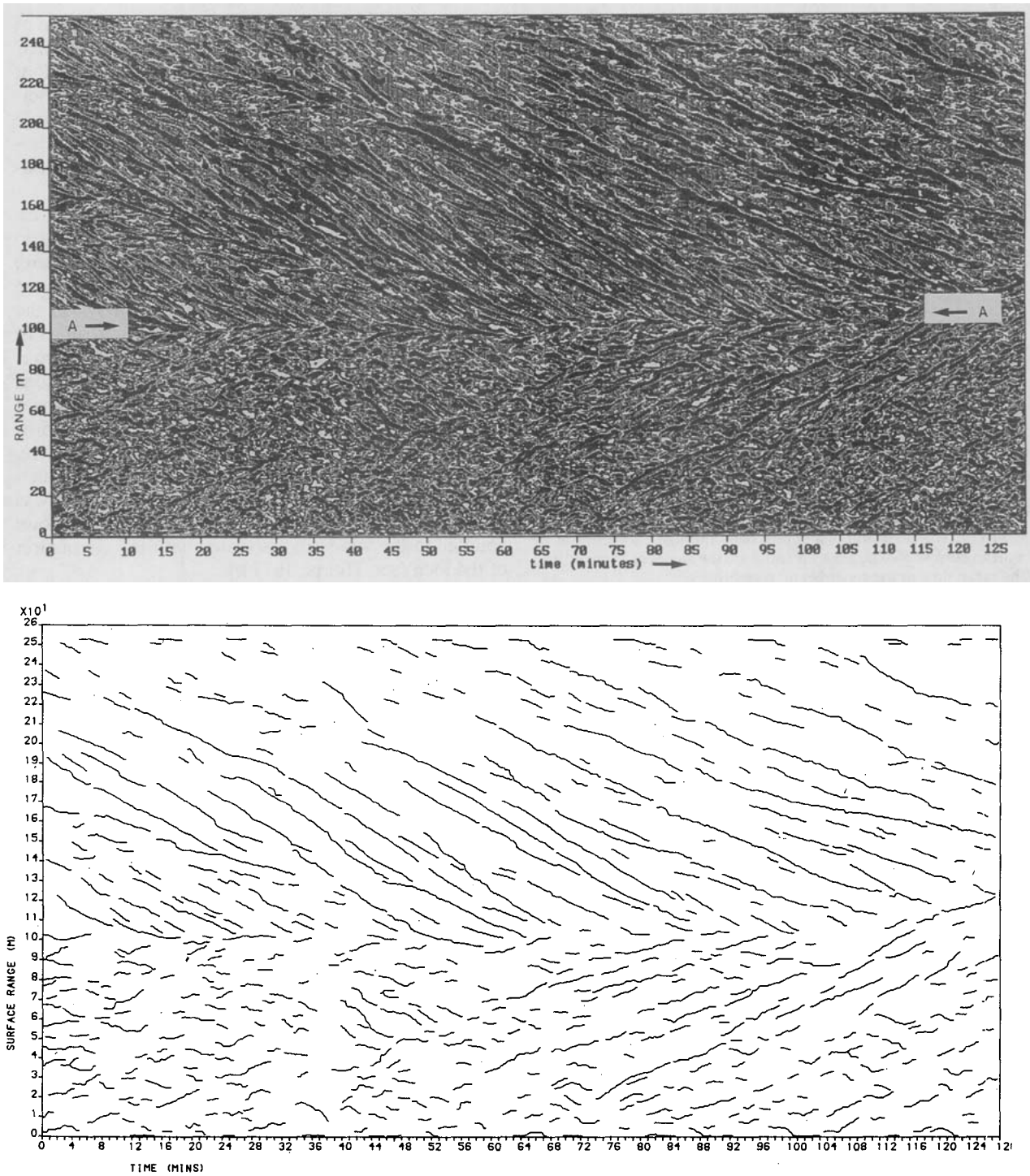

FIG. 5. (a) Sonograph (as in Fig. 1a) showing a front, made evident by the convergent motion of bands on its two sides. The point of zero range is 50 m from the sonar. The sonograph is produced by averaging pulses over 8 s. The temperature difference across the front is 0.2°C; $W_{10} = 8$ m s^{-1}. (b) The "skeleton" plot of the front.

of 10–20 made by Smith et al. (1987) for much larger convergence bands of scale l_s of 100–160 m in winds of 12–16 m s^{-1} in the open ocean.

Figure 8 shows a sonograph obtained in gusty winds. The bands are established within a time t_3 of about 3 min of a sudden change in wind speed, consistent with

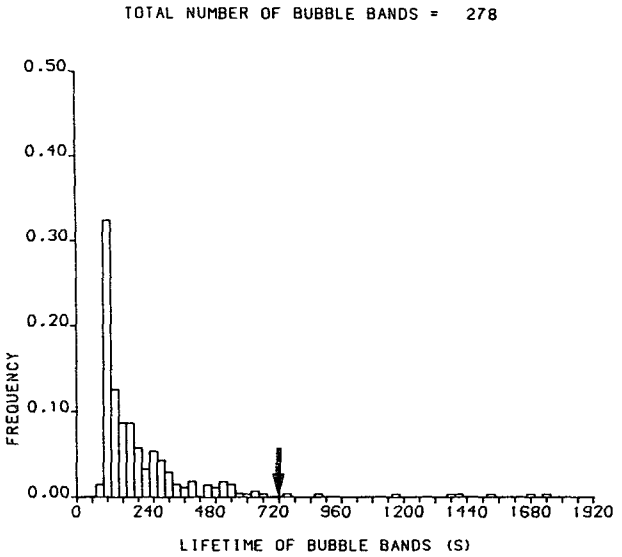

FIG. 6. Histogram of the times t_s for which bands are visible derived from the "skeleton" plot, Fig. 1b. The bin size is 60 s. The distribution has high positive skewness. The arrow marks the value T_s, the mean plus one standard deviation.

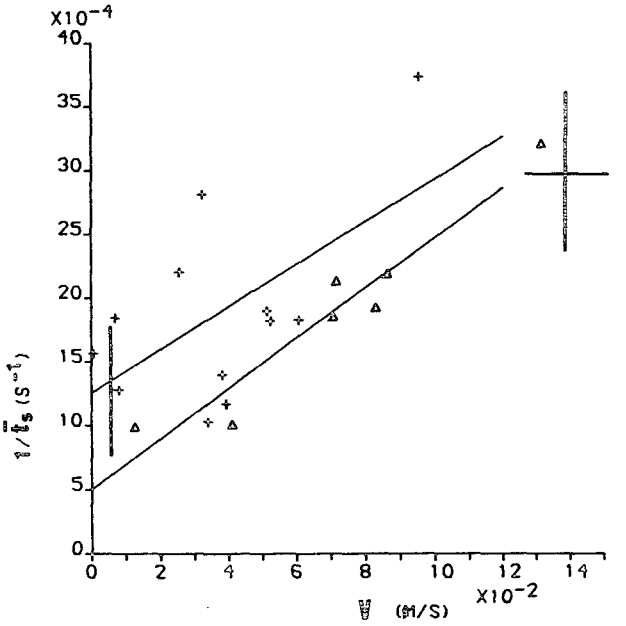

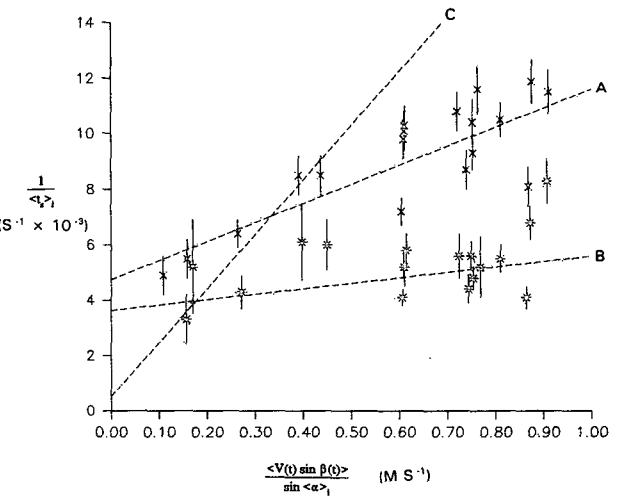

FIG. 7. (a) Loch Ness data showing values of T_s^{-1} versus the advection speed V. Points are the following: crosses, $W_{10} < 8$ m s^{-1} (average value 6.2 m s^{-1}); triangles, $W_{10} > 8$ m s^{-1} (average value 9.4 m s^{-1}). The error bars for T_s have been calculated using the extreme threshold limits (see caption of Fig. 3). (b) North Sea data showing plot of $1/\langle t_s \rangle_i$ against $\langle V(t) \sin\beta(t) \rangle / \sin\langle \alpha \rangle_i$, for $W_{10} = 9.5 \pm 0.5$ m s^{-1}. Crosses and regression line A indicate values for the full set of frozen field features, while stars and regression line B denote corresponding values excluding the shorter features. Regression line C is that of (a) for $W_{10} > 8$ m s^{-1} with linear extrapolation to higher currents. The errors reflect the sonograph temporal resolution limit and the standard errors associated with the ensemble mean and, for the longest lengths, the ensemble standard deviation. (Standard errors are appropriate for the North Sea data, as the frozen field reveals a homogeneous sample—and thus, it is assumed, population—of feature lengths.) The current data reference depth is 5 m (measured in the North Sea by an ADCP, on which the VAESAT was mounted, with a depth bin size of 1.4 m). The regression lines are used to estimate the lifetime τ and length L of the bubble bands.

earlier estimates (Leibovich 1983; Faller and Auer 1988).

b. Measurements in the North Sea

1) THE SIDE-SCAN SONAR AND ITS DEPLOYMENT

Upward-pointing side-scan sonars were deployed from a vessel anchored near 52°N, 2°E in the southern North Sea where the water depth is 45 m. A sample of the environmental conditions in which data selected for analysis were collected are listed in Table 2a. The water column is unstratified as a consequence of tidal mixing (Pingree and Griffiths 1978) and, unlike Loch Ness, there are M2 tidal currents that reach 1 m s^{-1}. A further practical difference is that the currents and winds are rarely parallel. An 80- and a 90-kHz transducer were mounted at right angles on a rig, and this was set on the seabed some 50 m upcurrent from the final anchor position of the vessel. The transducers were set to produce beams 90° apart in the horizontal. Each beam was directed up toward the surface at about 20° from the horizontal. The beams were 46° wide in the vertical and 2° in the horizontal (beam angles measured to the −3-dB points), directing sound toward strips some 2–5 m wide along the surface and away from the vessel. The rig was connected to the vessel by a cable that carried both power and the sonar signals. The latter were displayed in real time on a Waverley thermal linescan recorder and digitally recorded for subsequent analysis. [Further details of the sonar system are given by Thorpe and Hall (1994).] For most deployments, the current shear between the vessel and the rig was successfully employed so as to leave the 90-

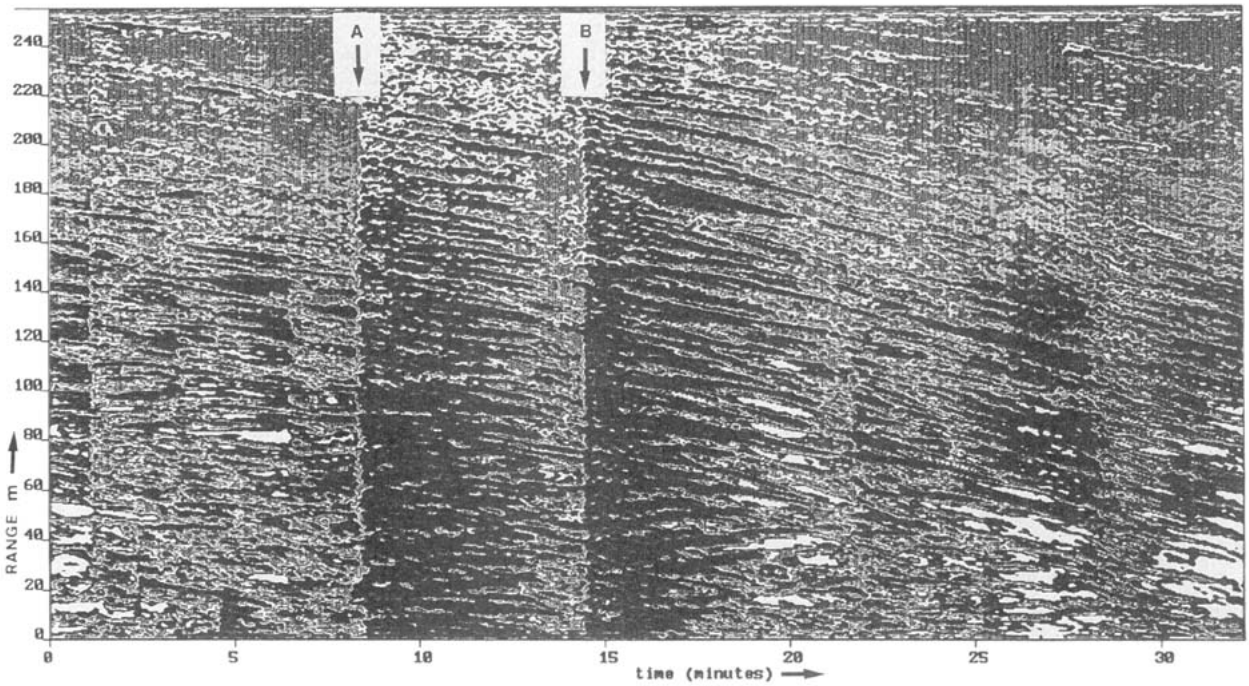

FIG. 8. A sonograph taken in Loch Ness during a period of gusty winds. The mean wind was 17 m s^{-1} but ranged from 11 to 23 m s^{-1}, with samples taken every 5 min. The vertical lines (e.g., at A and B) were observed to occur within 10–20 s of the onset of a gust. Viewing the sonograph from a low angle and from the left, it may be seen that bubble bands do not survive the onset of the gusts, but re-form between them in a time of some 3 min.

kHz sonar beam pointing nearly normal, and the 80-kHz beam nearly parallel, to the mean flow. Data are rejected in which wave or current directions were such that the water in the sonar beams may have been affected by the vessel. Measurements were made of wind speed (to ± 0.1 m s^{-1}) and direction (to $\pm 15°$) from the anchored vessel, giving 30-s average values.

As in Loch Ness, the cross-current sonograph shows strongly backscattering bands (Figs. 9a, 9b, and 10a; 9a shows the cross-current sonograph, and 9b that directed along current). Many of the features are linear and continuous, with a velocity component along the sonar beam close to v_y, the speed with which a straight bubble band advected passively by the current, V, would move (see Fig. 4):

$$v_y = V\frac{\sin(\alpha - \beta)}{\sin\alpha} \tag{7}$$

(v_y is positive for a band receding along the beam). When α is low (less than 30°–45°, over the range of current strengths observed in cross-current mode), bubble bands are swept sufficiently quickly through the beam for small-scale irregularities in the bands, and the tendency of the bands to meander (Thorpe and Curé 1994), to render the bands indistinguishable from isolated bubble clouds.

2) SKELETON PLOTS

Skeleton plots, shown as Figs. 9c and 10b, have been produced in a manner similar to those produced from the sonographs of the bands in Loch Ness (section 3a). For the strong tidal currents of the North Sea, the sonograph features are distributed densely over time, and the shape identification approach employed in skeletization necessarily involves a trade-off between clearly delimiting the features on one hand, and resolving features of the smallest length and timescales on the other. Furthermore, since the tidal current is not constant but at times changes steadily by as much as 1 cm s^{-1} min^{-1}, the skeleton images have been transformed by coordinate stretching to produce a two-dimensional spatial field, using data comprising 1-min averages from a 1-m depth VAESAT current meter moored within 1 km of the rig. The length and timescales of the class of features of interest and their direction relative to the sonar [α, following from (7)] and wind may thus be computed. To calculate inter-feature statistics such as the mean feature lateral spacing l_s, and times t_1, t_2, the features are approximated as "frozen" in the field over all time t, $t_0 \leq t \leq t_0 + \Delta t$, where t_0, Δt are the start time and duration of the sonograph, respectively. For a spectrum of features' lifetimes narrow about, and centered on, a characteristic lifetime τ, the frozen field approximation is invalid when taken over the whole field if $\Delta t > \tau$ but remains applicable for the computation of length and timescales smaller than $\int_t^{t+\tau} V(\xi)d\xi$, τ, respectively.

Values for $\langle t_s \rangle_t$ (see section 3a) have been computed for sections of the 2D fields over which changes in the

TABLE 2a. Environmental conditions and bubble-band scales of the North Sea data. The dates and times are days after 31 December 1990, and extend into 1992. Directions given are relative to the 90-kHz, broadly cross-current sonar beam, positive to its right, with the usual convention for wind direction, the direction *from* which the waves are coming, and the direction of current heading. Bounds shown in the data rows are measures of the spread over time, or equivalently, for the frozen field variables over space. In the case of the current, and wave height and period, this spread reflects systematic change, so the bound given is half the total change over the sonograph duration. For the wind vector and the frozen field, the spread typically reflects statistical fluctuation, so the bound given is the standard deviation. Bounds shown in the header rows are the standard error associated with a single measurement, given when greater or comparable to the temporal spread. The wind vector was measured by an anenometer and wind vane mounted at 18.2 m in 1991 and 9.8 m in 1992, and averaged over 30 s. Wind speeds are corrected to 10 m. The current vector was measured at 1-m depth by a VAESAT, profiled over the top half of the water column (depth about 45 m) by an ADCP, and sampled at 1/3 and 2/3 depths by two VACMs. The currents given are those as measured by the VAESAT, except for *1 values, which correspond to VACM data. Wave height and period of the dominant wave group were measured and averaged over hourly periods by a waverider buoy, except for *2 values, where measurements have been made from the sonar records (using data from a vertically pointing sonar also deployed). Wave direction was measured by eye. The measured mercury-in-glass air temperature ranged over the field work from 9.9° to 18.7°C, while that of the sea surface ranged from 9.5° to 17.3°C. The temperature of the air relative to the sea ranged from −2.8° to +2.9°C. Persistent heavy rain fell on Julian day 270. No precipitation was observed for the other datasets. Wind rows of foam were observed on Julian days 169 and 170.

Start (Julian day 1991)	Wind		Current		Waves			Frozen field features						
								Length (m)		Spacing (m)				
										Lateral		Longitudinal		
	W_{10} (m s^{-1})	Direction (±15°)	V (cm s^{-1})	β (°)	Height (cm)	Period (s)	Direction (±10°)	All	Long	All	Long	All	Long	α (°)
142.5913	5.5 ± 0.7	−129 ± 5	85 ± 10	84 ± 5	87 ± 10	3.9 ± 0.3	—	78 ± 37	149 ± 33	23 ± 18	34 ± 26	60 ± 114	415 ± 433	−95 ± 3
570.2495	5.9 ± 0.4	85 ± 3	64 ± 13	−40 ± 2	52 ± 2	3.1 ± 0.1	105	48 ± 24	81 ± 9	19 ± 14	17 ± 10	43 ± 71	390 ± 277	135 ± 4
573.7084	6.1 ± 0.7	78 ± 6	76 ± 1	113 ± 5	75 ± 3	4.0 ± 0.1	97	77 ± 35	137 ± 27	26 ± 20	30 ± 21	33 ± 92	353 ± 344	114 ± 4
169.4804	6.4 ± 0.8	−71 ± 8	80 ± 16	−84 ± 3	*2 35	*2 3.8	−93	32 ± 16	61 ± 11	26 ± 23	29 ± 31	18 ± 47	292 ± 378	−72 ± 9
570.2125	6.5 ± 0.3	83 ± 2	34 ± 18	−38 ± 6	49 ± 2	3.1 ± 0.1	105	38 ± 23	70 ± 10	13 ± 10	14 ± 11	10 ± 44	130 ± 157	127 ± 12
170.5210	7.2 ± 0.5	−70 ± 4	72 ± 13	−102 ± 3	89 ± 1	4.4 ± 0.1	−67	22 ± 10	38 ± 8	23 ± 16	30 ± 17	9 ± 24	90 ± 73	−78 ± 13
270.4722	8.9 ± 0.8	−84 ± 10	*1 84 ± 9	*1 107 ± 1	111 ± 2	3.7 ± 0.1	−66	79 ± 44	158 ± 29	21 ± 16	41 ± 28	39 ± 100	188 ± 238	−73 ± 4
617.6711	9.0 ± 0.5	−51 ± 28	26 ± 19	−103 ± 40	*2 70	*2 4.5	—	50 ± 24	87 ± 10	21 ± 17	44 ± 41	14 ± 57	67 ± 144	−66 ± 10
220.2449	9.8 ± 0.6	−93 ± 3	94 ± 2	120 ± 2	105 ± 4	3.6 ± 0.1	−81	74 ± 49	161 ± 52	29 ± 20	37 ± 24	23 ± 83	304 ± 306	−62 ± 3
220.3366	10.0 ± 0.7	64 ± 5	63 ± 17	−71 ± 3	120 ± 4	3.9 ± 0.1	86	61 ± 33	122 ± 25	27 ± 17	32 ± 34	29 ± 66	357 ± 510	106 ± 4
218.6710	10.0 ± 0.3	91 ± 5	71 ± 8	100 ± 2	70 ± 4	3.8 ± 0.1	83	58 ± 32	124 ± 34	27 ± 18	43 ± 24	15 ± 58	232 ± 202	105 ± 4

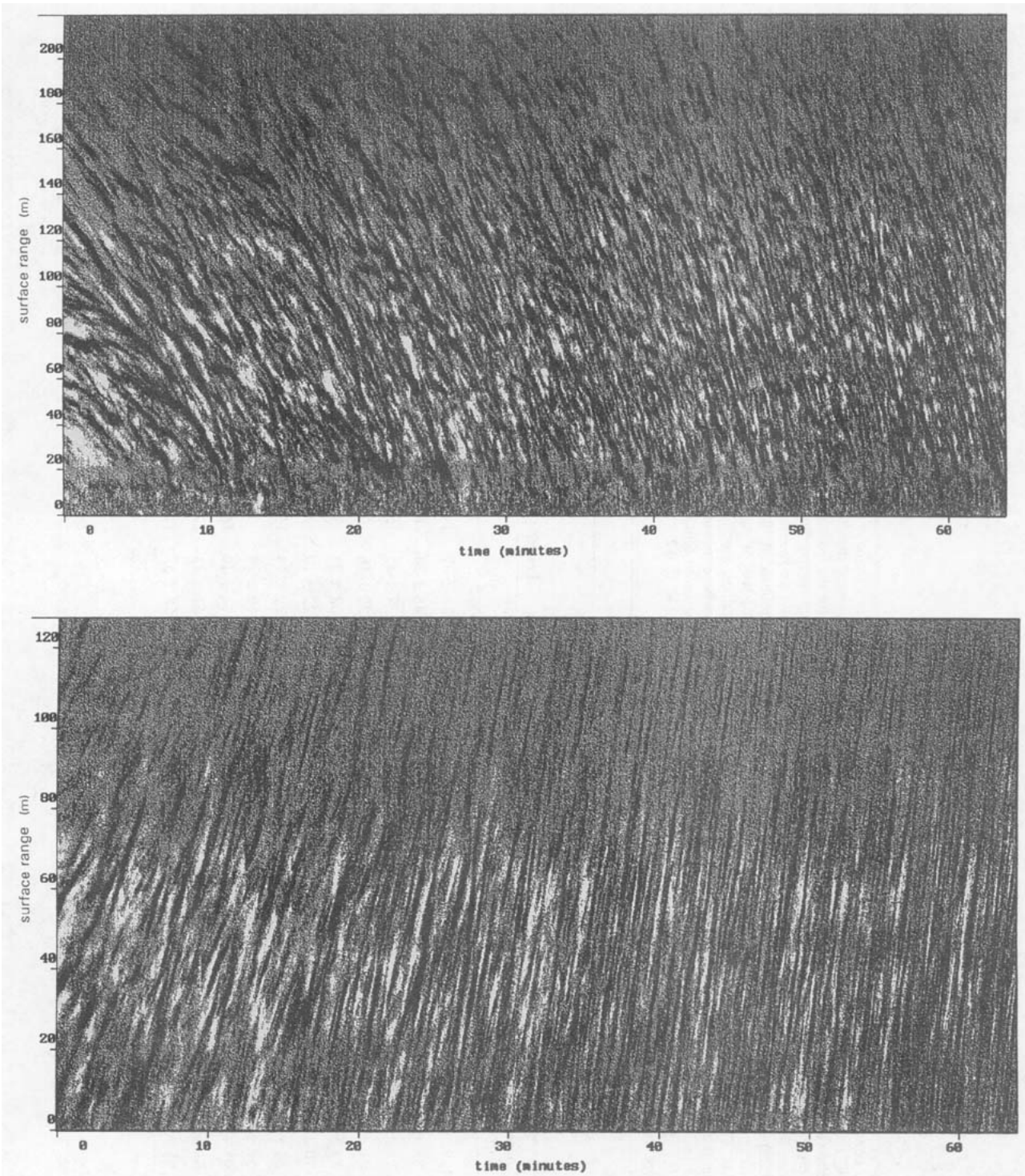

FIG. 9. Sonograph from the North Sea. Shading darkens with increasing backscatter. The pulse repetition frequency is 3 Hz, and averages of 12 are used to generate the sonograph. The environmental conditions are specified in Table 2a (the date is Julian day 617). (a) The 90-kHz component broadly cross current. This follows 10 min after slack tide, so that the current, and therefore the number of features advected past in a given time, are initially relatively low (current is 7 cm s^{-1}). Consequently, the left-hand region of the sonograph more closely resembles the sonographs of Loch Ness than at later times. The range origin is 17 m horizontally from the sonar. (b) The advection of individual bubble clouds away from the along-current 80-kHz sonar (from which the component of the current exactly parallel to the sonar may be measured). The sonar points 90° to the left of the cross-current sonar. The range origin is 32 m horizontally from the sonar.

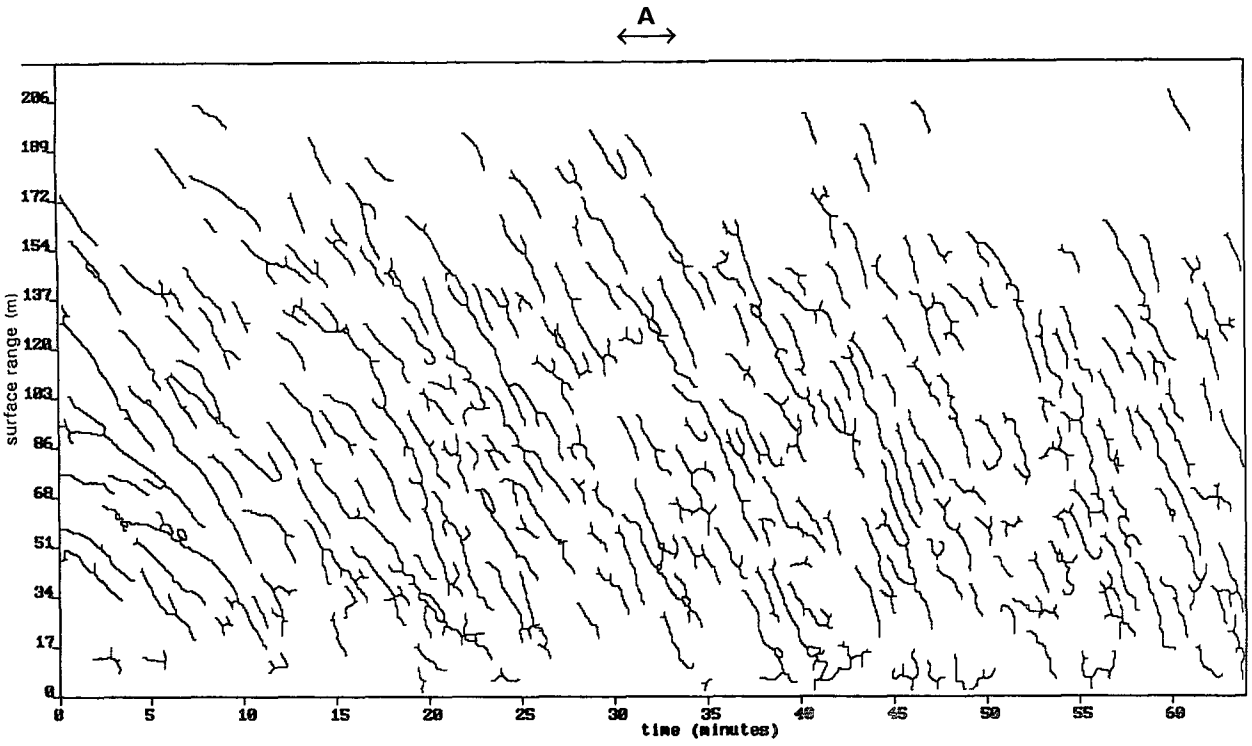

FIG. 9c. The skeleton plot of the cross-current sonograph (a). Line A indicates the duration in the beam, at that time, of a straight bubble band whose length is 50 m perpendicular to the beam, and whose lifetime is infinite. Features are skeletized that possess perimeters of 60 pixels or more, and whose average intensity lies within 25% of the most intense backscatter. (The threshold percentage is set higher than for the Loch Ness sonographs as there are more features in a given time.)

current and wind vectors are "small" (here $\langle\ \rangle_i$ denotes the average over an ensemble of i features). More specifically, the variation of $V(t)\sin\beta(t)$ about its mean $\langle V(t)\sin\beta(t)\rangle$ for a given section has limits of no more than ± 7 cm s^{-1}: the limits on the temporal change of the smoothed 10-m wind speed and direction were ± 0.5 m s^{-1}, $\pm 10°$, respectively. Each feature is first "linearized," ascribing it a spatially averaged length scale with an orientation by least-squares fit. For each field section, features that are highly nonlinear or "off wind" (lying more than one absolute standard deviation from the mean direction, as evaluated over the ensemble of i features) are then filtered out. The deviation of $\langle\alpha\rangle_i$ from the measured wind direction, on averaging over the ensemble of field sections, possesses a mean of 24° to the right of the wind, with standard deviation 20° (further details appear in Table 2a). Others have observed a tendency for wind rows to be aligned up to 15° to the right of the wind (see Pollard 1977); features offset at 20° are visible in the scanning sonar image of Farmer et al. (1993). Our estimate does not, however, necessarily imply a significant deviation from the measured wind direction. There is considerable uncertainty in the estimates of wind direction. A disparity between the near-surface current measured by the VAESAT and the advection velocity of the bubble bands could, from (7), alternatively be responsible. Such a disparity could arise because the advection velocity of the Langmuir cells, and hence that of the bubble bands, will be the mean current at some characteristic depth, and hence may differ significantly from that at the surface.

3) RESULTS, AND COMPARISON WITH LOCH NESS

Values for $\langle t_s\rangle_i$ have been estimated both for the complete set of field feature lengths and for a subset comprising those with lengths greater than the mean plus one standard deviation. A plot of $1/\langle t_s\rangle_i$ against $\langle V(t)\sin\beta(t)\rangle/\sin\langle\alpha\rangle_i$ for this subset appears in Fig. 7b, alongside the analogous data from Loch Ness. An error-weighted least-squares linear fit for the high wind speed North Sea data yields a gradient and intercept value that invert to yield $L = 505 \pm 341$ m and $\tau = 277 \pm 72$ s. The corresponding estimates on inclusion of the shorter feature lengths are 146 ± 25 m, 211 ± 33 s. The lower wind speed case is too scattered to permit a usefully accurate estimate of L, but is consistent with shorter lifetimes of 139 ± 108 s for the longest features, and 113 ± 56 s for the full set of feature lengths. The North Sea Langmuir circulation cells therefore appear to be longer but shorter lived than their Loch Ness counterparts. When the current is relatively weak, small discontinuities in the bands will be resolved (see section 3a). This is therefore a factor in

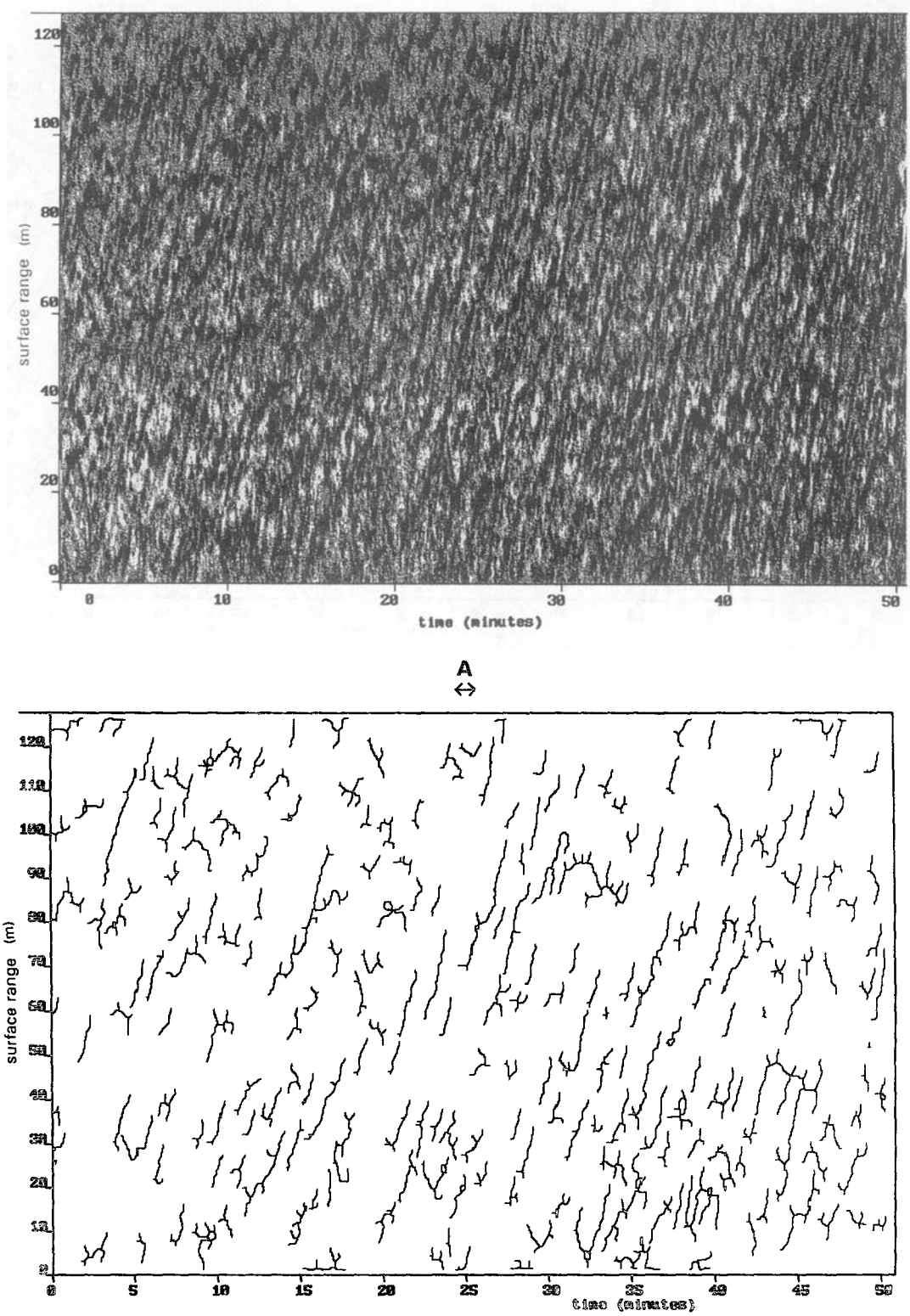

FIG. 10. Cross-current sonograph from the North Sea. The sonar pulse repetition frequency is 4 Hz, and the sonograph is produced by taking averages of 16 pulses. The range origin of the sonograph is 52 m horizontally from the sonar. The environmental conditions are specified in Table 2a (the date is Julian day 218). (a) The variety of patterns seen at large current speeds, including some of the nonlinear and discontinuous features. The band at about 53-m range is a result of interference with a separately running 250-kHz sonar. (b) The skeleton plot of (a). Line A indicates the duration in the beam, at that time, of a straight bubble band whose length is 50 m perpendicular to the beam, and whose lifetime is infinite. Features are skeletized as in Fig. 9.

the observed spectrum of lengths, and the inverse durations associated with the weaker currents in Fig. 7b may be biased upward with respect to the strong current values, depressing τ and inflating L.

A complementary length scale L' may also be computed by directly averaging the frozen field lengths over the ensemble of field sections. Table 2b shows these values, and those found for the mean feature lateral spacing l_s (by further linearizing about $\langle \alpha \rangle_i$), over the two wind speed regimes of Fig. 7a. Shown in Table 2b are the ensemble averages of the "longitudinal" mean spacing l_l between and parallel to the features:

$$l_l = \frac{1}{m_f l_s} - L', \tag{8}$$

where m_f is the frozen field feature density, the number of features per unit area. The mean feature lengths are less than half of those found graphically, consistent with the length "screening" effect of, and additional evidence for, a finite feature lifetime. The lateral spacings exceed those at comparable wind speeds in Loch Ness (Fig. 3). The aspect ratio L/l_s in winds of about 9.5 m s^{-1} is estimated to be 13 ± 9 for the longest features, similar to Smith et al.'s (1987) estimates of 10–20 but falling to 6 ± 2 when features of all lengths are included.

Convergence speeds into the bands may be estimated from the sonographs as in section 3a. Allowing for variation of α from 90°,

$$u = |(v_y^m - v_y) \sin\alpha|, \tag{9}$$

where v_y^m is the velocity component along the sonar beam of the transient, marker band. The errors in the estimation of u are, however, much higher for the North Sea than for Loch Ness; as well as the introduction of errors associated with α, the strong currents cause poorer effective spatial resolution perpendicular to the sonar, an important limitation for measuring transient bands of short length and lifetime. Measurements were limited to currents normal to the sonar beam less than 20 cm s^{-1}, itself a tight restriction on the admissible data to that lying within 30 min of a slack tide. A value of 16 ± 8 cm s^{-1} for winds of 6–9 m s^{-1} has been obtained. (The North Sea dataset was too small to look for a wind speed dependence.) Given the values of l_s from Table 2b, comparison with Figs. 2 and 3 (and the constraint that $\tau > t_1 = l_s/u$ for the formation of the bands) therefore offers evidence that convergence speed and band separation in the North Sea are at least twice those in Loch Ness. We return to discuss the implications in section 5.

TABLE 2b. Values averaged over two wind speed regimes (the higher regime is that of Fig. 7b).

	Frozen field features					
			Spacing (m)			
	Length (m)		Lateral		Longitudinal	
W_{10} ± 0.5 (m s^{-1})	All	Long	All	Long	All	Long
6.3	49 ± 23	87 ± 45	22 ± 5	26 ± 7	27 ± 15	256 ± 117
9.5	63 ± 15	128 ± 37	25 ± 3	39 ± 4	27 ± 15	256 ± 117

4. Dispersion of floating particles

a. The model

A deterministic model has been developed to simulate horizontal dispersion due to Langmuir circulation. The model is similar to those of Faller and Auer (1988) and Thorpe and Curé (1994), in that floating particles or "tracers" converge toward, and move within, nonsteady bands. It differs from Faller and Auer's in that the bands are derived from real data, the sonographs, in which bands form, expire, and join. The model differs from Thorpe and Curé's in which the tracers were constrained to lie along the line defined by the sonar beam. Here tracers are advected by the current and are free to disperse longitudinally. The dispersion of tracers over timescales of between 2 min to 1 h, and hence, in the tidal currents, over (longitudinal) distances of 50 m–2 km, is computed by Monte Carlo simulation using the North Sea sonar data. The tracers are "released" at time t_0 from a subset of grid points over the "skeletized frozen field" (without prior filtering of nonlinear or off-wind features), chosen so as to both optimize the time each tracer spends in the field and to keep the tracer density broadly constant. Simulations have been run with the tracers released in batches, with each batch released instantaneously over many points in the sonar beam, and with large intervals of time separating batches; or with frequent releases from a fixed point in the beam. The former case—"absolute" dispersion—has been used to compute the dispersion statistics presented in section 4c.

Each tracer's subsequent motion is composed of the vector sum of its motion relative to the field and the motion of the field relative to the sonar as the field is advected past by the mean current. Tracer motion relative to the moving field is shown in Fig. 11. Before reaching a skeleton line this tracer motion consists of

(i) drift at the surface relative to the features. Each tracer in the frozen field frame is assigned a velocity component that is both parallel to, and a selected (and later specified) small fraction c_w of the wind vector associated with the frozen field at the tracer's location.

(ii) a velocity component u_p perpendicular to the wind, directed toward the nearest feature to the tracer, to reflect Langmuir circulation convergence. A linear dependence on wind speed is prescribed. [Occasions may arise, for example, near the edge of the frozen field, when there is a feature on only one side of a tracer—that is, to the left or right of the wind, and not

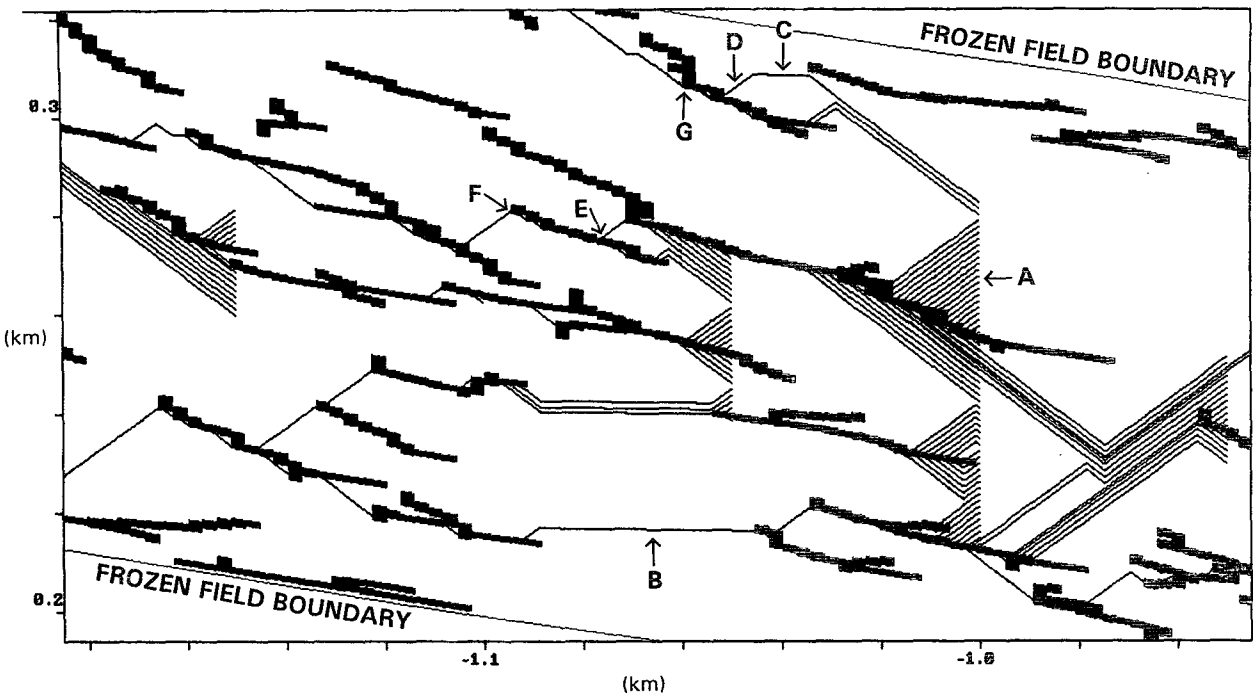

FIG. 11. Tracer movement with respect to frozen field features, illustrating the degree of convergence induced by the Langmuir circulation, with the model input parameters set at their reference values. (The thickness of the frozen field skeleton features has been exaggerated by a factor of 10, to distinguish them from the tracers.) The cross-current sonar is situated out of picture at the origin and directed along the y axis. The field is generated from Fig. 10b between t = 24 min 13 s and t = 29 min 57 s, and is shown at its position at t_0 (see section 4a). Point A marks an instantaneous "burst" release of tracers, with the number released determined by the requirement that the tracer density be kept broadly constant. Points B–G are referred to in section 4a. Tracers drift to the left.

simultaneously to both—or when there are no features at all. In such cases, unless the distance from a tracer to a feature is less than half the wind row spacing (e.g., Fig. 11, point D) the value assigned to u_p is zero (e.g., Fig. 11, points B and C). This prevents net tracer inflow at the frozen field boundaries.]

Once a tracer reaches a skeleton line it is captured (Fig. 11, point E), and c_w is inflated by a specified amount to reflect the stronger downwind current in the vicinity of a wind row. The tracer then remains captured until it reaches the end of the feature (Fig. 11, point F), or until the feature develops an off-wind orientation greater than $\tan^{-1}(u_p/c_w W_{10})$ (Fig. 11, point G), or until the time for which the tracer has "preferred" the feature over any other exceeds a prescribed lifetime T_p. On exiting, or ceasing to be aligned with, a skeleton feature, the tracer moves as in (i) and (ii). The setting of c_w, u_p, and T_p and the sensitivity of the model to these values is addressed in sections 4b and 4c.

The tracer thus moves iteratively in constant-velocity steps until either it leaves the field, or $t - t_0$ exceeds the maximum dispersion time considered, Δt (see section 3b). The calculation of the horizontal dispersivity follows from the first and second moments of the ensemble excursions of the tracers from their respective starting points at t_0 (the ensemble excursions associated with Fig. 11 are shown in Fig. 12). These statistics are generated longitudinally and laterally to the mean tracer flow. Tracers are effectively reintroduced into the field where necessary, to ensure that each Monte Carlo run takes place over the full dispersion time Δt. Segments of the excursions for which u_p is zero are discarded (and the dispersion time correspondingly frozen), as these understate dispersion. Such segments occur at the frozen field boundaries, toward which tracers tend to migrate, and also during any regions of missing data. (This mechanism is also used to implement the finite lifetime T_p input to the model. Once the time for which a tracer has preferred a feature exceeds T_p, the subsequent excursion is discarded, until a new feature is encountered.)

b. *The selected sensitivity values*

The selected reference input parameter values are a lifetime T_p = 20 min and a convergence speed u_p following from the Loch Ness relation (4). We select a drift factor c_w = 0.5% of W_{10}, rising to 0.8% within a (skeletonized) feature. Four other scenarios were considered, in order to establish sensitivity, each differing from the reference set in only one variable. A low-lifetime scenario was considered, with T_p = 10 min, to reflect the evidence of section 3b that the North Sea

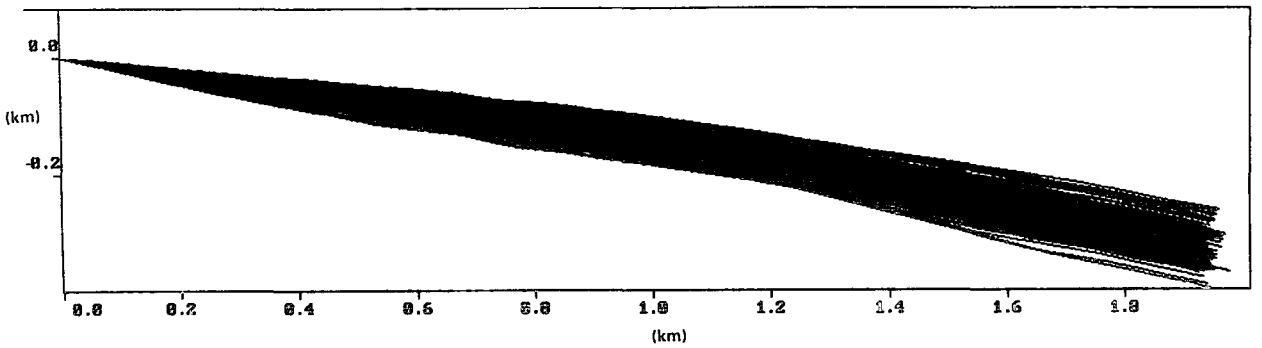

FIG. 12. The excursions of tracers from their release points, as shown in the (inertial) sonar frame. This illustrates the degree of dispersion induced by the Langmuir circulation, superimposed on the strong tidal advection. The model input parameters are set at their reference values. The skeletized sonograph used by the model is that of Fig. 10b (the tracer motion in the frozen field is shown in Fig. 11), with the averaged wind and current data given in Table 2a (Julian day 218).

bubble band lifetimes are smaller than for Loch Ness. Two extremes of downwind drift were studied: a low-drift case where $c_w = 0\%$ of W_{10}, rising to 0.1% within a feature; and a high-drift case, where $c_w = 1.5\%$ of W_{10}, rising to 2.5% within a feature. Estimates of wind-induced drift lie between 2%–4% of W_{10} (Wu 1975), but a contribution from the wind-induced current already enters the model when the frozen field is generated using the 1-m depth VAESAT measurements. Finally, a high-convergence-speed case was considered, reflecting the evidence of section 3b that convergence speeds in the North Sea are higher than in Loch Ness, with u_p following from a doubling of the coefficient of W_{10} in (4).

The general behavior of the tracers was measured by recording the mean percentage of time tracers spend captured in features, p_c, and the mean number of features encountered in time T_p per tracer, n_f. The mean number of reintroductions into the frozen field in time T_p per tracer, n_r (see section 4a), was recorded: the relative importance of the "artificial" contribution to the tracer's excursion so induced may be gauged by the ratio $\kappa_r = n_r/n_f$ (essentially the number of reintroductions per feature encountered). Similarly, the relative importance of lifetime was assessed by recording n_e, the mean number of features to expire in time T_p, and then computing $\kappa_e = n_e/n_f$ (essentially the number of features expiring per feature encountered).

c. *Results*

1) THE RESPONSE OF THE MODEL TO SELECTED VALUES

The model was run using data from two summers of field work (see Table 2a), and over the range of scenarios (section 4b), so as to establish model sensitivity. Analysis of the results will be limited to establishing their broad dependence on the input parameters and on wind speed.

The mean values of p_c, n_f, n_r, and n_e, averaging over the set of selected sonographs, contribute to Table 3. Comparing the low lifetime to the reference statistics, we see that, as expected, lowering the lifetime on average decreases the proportion of time that tracers spend captured. That n_f is not halved along with the lifetime is because the rate at which tracers "see" new features is increased, with the difference largely accounted for by the increase in the rate at which wind rows expire. In the low-drift scenario, with zero downwind drift outside features, the proportion of time that tracers spend captured is much larger. As the drift within a feature over the maximum dispersion time (about 1 h) is around half the mean feature length (see Table 2), p_c would be higher still were it not for the dispersion induced by T_p, which the relatively high value of κ_e indicates is important. As κ_r is unity, the artificial dispersion caused by tracer reintroduction

TABLE 3. Model output, showing sensitivity of the estimated values to the input parameters.

Specification	T_p (min)	W_{10} coefficient of u_p (10^{-3})	c_w in-out features (%) In	Out	p_c (%)	n_f	κ_r	κ_e	m [$K(t) \propto t^{m-1}$], for $W_{10} \pm 0.5$ (m s^{-1}): 6.3	9.5	n ($K \propto W_{10}^n$ at t = 45 min)	K (t = 45 min) (cm^2 s^{-1}), for W_{10} (m s^{-1}): 5	10
Reference	20	3.42	0.5	0.8	20 ± 16	3.0 ± 0.8	0.29 ± 0.09	0.06 ± 0.05	1.19 ± 0.11	1.19 ± 0.11	1.07 ± 0.89	400 ± 950	830 ± 2330
Low T_p	10	3.42	0.5	0.8	18 ± 13	1.8 ± 0.3	0.29 ± 0.07	0.26 ± 0.09	1.19 ± 0.09	1.19 ± 0.09	2.09 ± 0.56	260 ± 400	1100 ± 1960
Low c_w	20	3.42	0	0.1	69 ± 4	1.5 ± 0.1	1.00 ± 0.31	0.52 ± 0.07	1.27 ± 0.08	1.09 ± 0.08	1.12 ± 0.70	420 ± 770	920 ± 1990
High c_w	20	3.42	1.5	2.5	4 ± 4	9.5 ± 3.6	0.18 ± 0.10	0.00 ± 0.01	1.29 ± 0.17	1.54 ± 0.16	5.17 ± 1.51	60 ± 240	2220 ± 10 290
High u_p	20	6.84	0.5	0.8	49 ± 18	2.8 ± 0.8	0.30 ± 0.09	0.08 ± 0.05	1.06 ± 0.13	1.06 ± 0.13	2.23 ± 0.64	360 ± 630	1700 ± 3450

might also appear important. This results, however, from tracers leaving features adjacent to the frozen field boundaries; the tracer velocity in the frozen field becomes zero, and reintroduction ensues. Reintroduction therefore takes place just when the tracer would have begun converging to a new feature, were the frozen field unbounded.

In the contrasting high-drift, case tracers are rarely captured for long (i.e., p_c is generally small). Very few features expire because the tracers drift through the portion of each feature's length to which they are exposed before the lifetime limit (20 min) is reached, for all but the very longest features (see Table 2b). For the high-convergence-speed scenario, the proportion of time spent captured relative to the reference value is more than doubled, due both to the increased rate at which a tracer converges and to the correspondingly enhanced probability of it converging successfully before the feature toward which it is heading terminates in space or time, or another feature intervenes.

The general tendency of p_c is to increase with wind speed. This is most clearly apparent in the low-drift scenario, where any differences $\Delta\theta$ between the orientation of wind and bubble bands is least important. The trend can be ascribed to a tendency for the mean frozen field feature length to increase with W_{10} (see Table 2). With the exception of the low-drift case, this increase is also sufficiently marked to cause n_f generally to decrease with increasing W_{10}, despite the higher drift (both in and outside features). At a given wind speed, the effect of increasing $\Delta\theta$ is to reduce p_c and increase n_f, the effects least and most marked for the low- and high-drift scenarios, respectively. Much of the scatter at fixed W_{10} observed for p_c and n_f may result from the scatter of mean feature length and $\Delta\theta$.

As the tracers, when released, are at positions uncorrelated with the frozen field features, they will at time t_0 lie on average a distance $l_s/4$ laterally from the nearest feature, and will begin converging toward it with speed $u_p \cos\Delta\theta$. We therefore monitored the quantity γ, defined by

$$\gamma = \frac{4u_p \cos\Delta\theta t_f}{l_s}, \tag{10}$$

where t_f is the mean time that elapses before a tracer is captured for the first time. We should expect (10) to satisfy $\gamma \geqslant 1$, the inequality resulting from the generally finite probability of tracers "seeing" more than one feature before capture for the first time. In the special case where the drift outside features is zero, γ should achieve its lower bound. The observed values $\gamma = 0.93 \pm 0.11$ for the low-drift scenario, and $\gamma = 1.31 \pm 0.12$ as averaged over the other scenarios, statistically confirm these predictions.

2) Lateral dispersion

An example of the lateral dispersion curves that result from the sensitivity analysis is shown in Fig. 13. The large initial dispersion for the high-convergence-speed case is because the time for first capture is smaller than for the other cases; as dispersion time progresses, the relative importance of the first event diminishes. Statistically significant differences between the reference and low-lifetime cases start at $t = 600$ s, the value of the low lifetime assigned to T_p. The gradient of each logarithmic plot reveals the power index M of time on which the lateral variance σ^2 depends; M tends to take its maximum (smoothed) value for times up to the timescale of the first capture, and thereafter is smaller. The variance, however, clearly remains dependent on time up to the maximum dispersion time considered.

The lateral dispersivity K, defined as

$$K = \frac{1}{2}\frac{d\sigma^2}{dt}, \tag{11}$$

has been computed both for the polynomial dependence of variance on time [that is, $M \equiv f(t)$], and by monomial approximation,

$$\sigma^2 \sim \propto t^m \tag{12}$$

($M = m$ is a constant). In all the sensitivity scenarios, the dispersivities show a broad tendency to increase with increasing wind speed. This relationship has thus been assessed further, by fitting $K(t = 2700\text{ s})$ to W_{10} by monomial approximation:

$$K\,(t = 2700\text{ s}) = AW_{10}^n. \tag{13}$$

The values of $K\,(t = 2700\text{ s})$ used to implement (13) are those following from the (better) polynomial fit of variance to time, but are error weighted, using either the error from the monomial fit of variance to time, or the absolute bias between the two fits at $t = 2700$ s, whichever is the larger. In this way, we accord low weight to dispersivities from datasets where M changes markedly before $t = 2700$ s, as this reveals features of the dispersive process specific to the particular dataset, and to the locality of the chosen dispersion time.

Why should the dispersivity tend to increase with W_{10} across the wide variations of lifetime, drift, and convergence speed considered? From section 4c.1, it is known that the proportion of time spent captured, p_c, tends to increase with W_{10}, which might by itself be thought to inhibit dispersion. There are, however, other factors that act in opposition to this: the convergence speed increases with increasing wind speed, as, aside from the low-drift case, does the time per feature T_p/n_f for ensemble dispersion to take place (see section 4c.1). It must also be borne in mind that dispersion longitudinal to the features resulting from the higher downwind drift imparted to tracers once captured will affect the dispersion lateral to the mean tracer flow, the measured dispersion, for two reasons. First, the orientation of the lateral axis computed when measuring the dispersion will not lie perpendicular to the features, except in the special case where the orientations of the

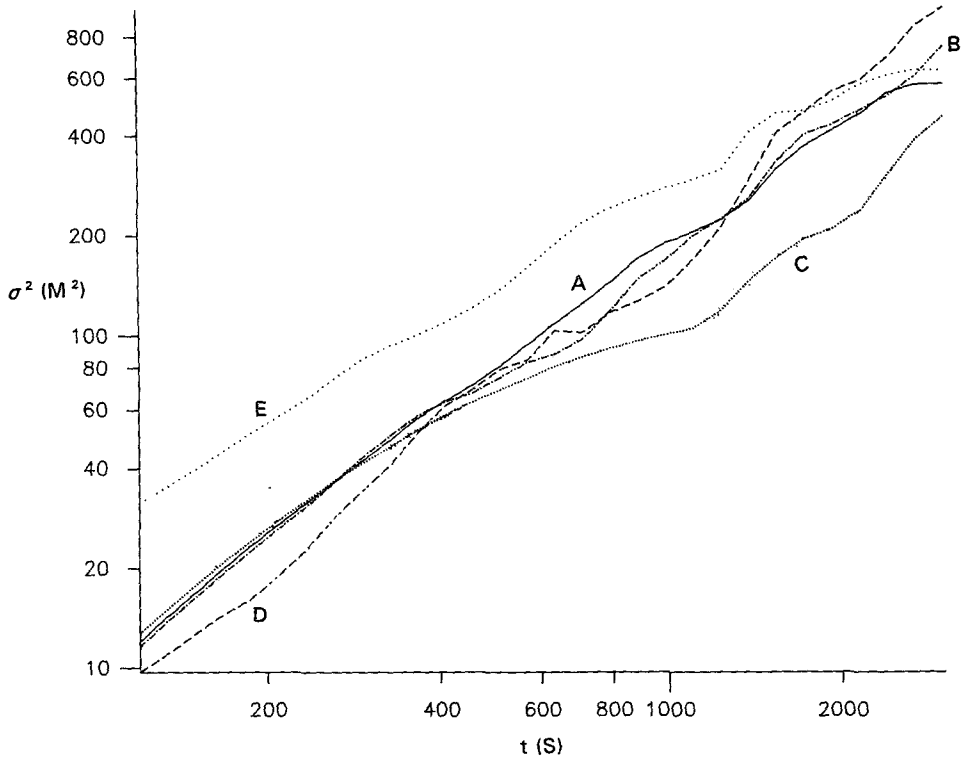

FIG. 13. The dependence of the lateral variance σ^2 of tracers' excursions on dispersion time t for the five input parameter settings used to evaluate the sensitivity of the model. Curves A–E denote the reference, low-lifetime, low-drift, high-drift, and high-convergence current scenarios, respectively. The environmental conditions are given in Table 2a (Julian day 218), and the excursions are shown in Fig. 12, with the input parameters possessing their reference values.

current, wind, and features all concur. Second, dispersion longitudinal to the features directly enhances its lateral analog, by broadening the spectrum of times over which a given feature interacts with tracers. This latter effect will increase with increasing wind speed. The tendency of bubble bands to meander about their mean axes (Thorpe and Curé 1994) will ensure that lateral dispersion is always taking place, whether a tracer is captured or not.

The mean values of m, n, and K, found by averaging over the set of selected sonographs (and with K evaluated at $t = 45$ min using 13), for two reference wind speeds appear in Table 3, and from this we draw the following conclusions. The reference dispersion is characterized by a power of time that, to monomial approximation m, is independent of the wind speed; and by a dispersivity after 45 min that, to monomial approximation, is broadly proportional to the wind speed (i.e., $n = 1$). In the low-drift case, the 45-min dispersivity is similarly broadly proportional to wind speed, with a slightly higher coefficient of proportionality. However, the power of time following from monomial approximation, m, tends to fall off with increasing wind speed. The dispersion in the low-drift scenario is larger than those in the other scenarios at low wind speeds and dispersion times.

The remaining sensitivity scenarios all yield dispersivities that increase with the wind speed to higher powers. Lowering the lifetime or raising the downwind drift speed from its reference value depresses dispersivity at low W_{10}, and enhances it at high W_{10}. These effects are most marked in the high-drift scenario, for which m also has a tendency to increase with W_{10}. Raising the crosswind convergence speed tends to enhance the dispersion, particularly for high winds and low dispersion times, when the effect of a relatively speedy first capture is most important.

The dispersivities encountered range over two orders of magnitude, broadly from 5×10^{-3} to 0.5 m^2 s^{-1}. Comparitive values of Csanady's estimate (1), over wind speeds of 5–10 m s^{-1}, on using a lifetime of 20 min and values of lateral spacing from Table 2b, range from 0.4 to 0.5 m^2 s^{-1}. Comparative values of Faller and Auer's meandering model relation (3), over the same range of wind speeds and lateral spacings, and choosing u according to the Loch Ness relation (4), range from 1.7×10^{-2} to 2.6×10^{-2} m^2 s^{-1}. We note that Faller and Auer's numerical diffusivities tally best with their analytical prediction (3) over timescales of 80–160 min, but for shorter times are considerably larger, and closer to our numerical results. A better analytical approximation to both the midrange and

spread of the dispersivities we have computed, follows from supposing the lateral dispersive process to induce an excursion $\pm [(1 - 0.01p_c)u_p \cos\Delta\theta](T_p/n_f)$ with frequency n_f/T_p, yielding

$$K = \frac{[(1 - 0.01p_c)u_p \cos\Delta\theta]^2 T_p}{2n_f}, \qquad (14)$$

where $(1 - 0.01p_c)$ represents the fraction of time particles are migrating between the sonograph features, $u_p \cos\Delta\theta$ is the particle convergence speed, T_p is the feature lifetime, and n_f is the mean number of features encountered by particles in time T_p. Using the same database as the model, this yields estimates for K of between 1×10^{-2} and 0.2 $m^2 s^{-1}$.

5. Discussion

Sonar has been used to derive space and time estimates of Langmuir circulation, which provides an important process of near-surface dispersion on scales of 2–200 m and on timescales of 1 min to a few hours. The principal conclusions are as follows.

1) It is evident from the sonograph records and skeleton plots that, at scales of 2–200 m, the acoustic scattering field is not isotropic. We conclude that the patterns of convergence and the two-dimensional turbulence at the surface, each related to the three-dimensional structure of mixed layer turbulence that includes Langmuir circulation, are not isotropic. This conclusion is consistent with other measures of isotropy in the mixed layer at these scales [e.g., the skewness of the horizontal derivative of temperature; Thorpe et al. (1991)].

2) We have made estimates of the scales of the patterns found in the sonograph records, the speeds at which floating material is drawn into the convergence lines, and the lifetime of linear features in both Loch Ness and in the North Sea. These are summarized in Figs. 2, 3, and 7, and in Table 2, and are related to wind speed. A key parameter in determining the effectiveness of Langmuir circulation in producing convergence and its role in the coherent patterns of turbulence in the upper ocean is $\tau u/l_s$, the lifetime divided by a measure of the circulation time of water particles in the cells. The value of this parameter in Loch Ness is 1.5 and 4.8 at mean wind speeds of 6.2 and 9.4 m s^{-1}, respectively, emphasing the relatively greater continuity of the bands at higher wind speeds.

3) There are significant and intriguing differences between the data from Loch Ness and the North Sea, most vividly displayed in Fig. 7. If the assumption made in section 3 that the lengths and lifetimes of the convergence bands or wind rows depend only on forcing conditions characterized by the wind speed, then the slopes and intercepts of the points in Figs. 7a and 7b in similar wind speeds should be the same. They are not. The inferred lifetimes in Loch Ness are longer, and longer bands with greater separation occur in the North Sea. The points in Figs. 7a and 7b do, however, converge in their region of overlap where the advective currents are about 14 cm s^{-1} (Fig. 7b). This fact suggests that the lower slope of the North Sea data at higher currents is not the result of the possibly shorter-lived clouds of faster rising bubbles in the freshwater loch (see Scott 1975), and therefore by less continuous bands, but that it is more likely to be caused by a component of forcing, or dissipation, absent in Loch Ness, which leads to the less regular structures and a greater prevalence of large-scale features in the North Sea, although with short durations. While the bias mentioned in section 3b toward large scales resulting from the resolution problems at high current advection speeds is a contributing influence, the longitudinal spacing or mean "gap" between features is at least half the mean feature length (see Table 2b), suggesting that the influence of small regions in which bubble clouds are absent is insufficient to account for the different slopes. The influence of longer period waves in the longer-fetch North Sea, typically 3–5 s (Table 2) compared to 1.5–4 s in Loch Ness, may affect the scale of the circulation patterns. A scaling of the width of the cells with the wavelength of surface waves is predicted by Leibovich and Paolucci [1981; but see also Smith (1992)]. Wavelengths are proportional to the wave periods, so perhaps accounting for the lower slopes in Fig. 7 and the larger scales of the North Sea data.

This does not, however, explain the shorter lifetimes. It appears that another effect is important. The water column is unstratified in the southern North Sea. The North Sea skeleton plots have a greater content of nonlinear and off-wind direction components than those from Loch Ness. Evidence of sediment-laden eddies with scales of 10–100 m, probably caused by turbulence generated by the strong tidal current flow over the seabed, is visible in video photographs taken from aircraft in the area as part of our collaborative studies (T. Lunel 1992, personal communication). The coherence scales of the horizontal velocity field in the water column during strong tidal flows have been measured using an array of moored current meters by S. R. Shield and A. J. Elliott (1994, personal communication) and are found to be approximately equal to the water depth. The effect of turbulence produced by the stress of the tidal flow over the seabed, a factor absent in Loch Ness, will lead to the generation of nonlinear patterns of convergence and divergence on the sea surface, and a rapid distortion and possible reduction of small-scale linear features generated by wind-wave action by rotating and decorrelating them from their forcing. This will contribute to a prevalence of (surviving) larger-scale structures. The turbulence will, however, also lead to the more rapid breakup of even the larger linear features and a consequent overall reduction in the pattern lifetime. Bottom-generated turbulence may therefore contribute to the dispersion of floating material

in two ways. It will produce dispersion even in conditions of no surface forcing. The associated dispersion coefficient, in a constant stress layer proportional to u_*z (u_* is the friction velocity), will increase with tidal current and with water depth. In windy conditions when the Langmuir circulation is present, bottom-generated turbulence will tend to promote more transient patterns of near-surface circulation, as found in the data from the North Sea, and hence enhance the rate of spread controlled by Csanady's mechanism of Langmuir circulation breakup. Our present estimates of dispersion may therefore be valid only in currents and waters of depth similar to those of the measurement area in the southern North Sea, namely about 45 m.

4) Estimates of the diffusivities show an increase with wind speed, but are sensitive to the choice of underdetermined parameters (Table 3). Further discussion of the competing effects of Langmuir circulation and bottom-generated turbulence and a comparison with observations of oil dispersion are deferred to a later paper. Preliminary comparisons suggest that the sonar estimates in section 4 can account for much of the observed dispersion. The sensitivity of the estimates of dispersion to the selected parameters, however, indicates that more research is needed in their measurement if less empirical models are to be developed. The models are presently being extended to apply to soluble substances and to explain the different rates of diffusion of buoyant and dissolved material. A longer-term objective is to provide a parameterization of the effects of Langmuir circulation that could be used to model dispersion in shallow seas or the upper ocean.

Acknowledgments. The experiments in Loch Ness were funded by the U.K. NERC and by the U.S. Office of Naval Research under Grant N00014-90-J-147. The observations in the North Sea form part of an EEC-funded MAST project in collaboration with the DTI Warren Spring Laboratory and the Institute of Oceanographic Sciences Deacon Laboratory, which obtained and kindly provided the VAESAT current meter data. We are grateful for this collaboration, particularly to the Master and Crew of *Sea Spring* from which vessel the North Sea experiments were made. We are grateful to Dr. A. Elliott for showing us his results with Mr. Shield on correlation scales prior to publication. A preliminary report of this work was submitted to the International Conference on Physics of Estuaries and Coastal Seas, Margaret River, West Australia, 8–10 December 1992.

REFERENCES

Brtko, W. J., and R. L. Kabel, 1978: Transfer of gases at natural air–water interfaces. *J. Phys. Oceanogr.*, **8**, 543–556.

Brumley, B. H., and G. H. Jirka, 1988: Air–water transfer of slightly soluble gases; turbulence, interfacial processes and conceptual models. *Phys. Chem. Hydrodyn.*, **10**, 295–319.

Crawford, G. B., and D. M. Farmer, 1987: On the spatial distribution of ocean bubbles. *J. Geophys. Res.*, **92**(C8), 8231–8243.

Csanady, G. T., 1973: *Turbulent Diffusion in the Environment.* Reidel, 248 pp.

——, 1974: Turbulent diffusion and beach deposition of floating pollutants. *Advances in Geophysics,* Vol. 18A, Academic Press, 371–381.

Faller, A. J., and S. J. Auer, 1988: The roles of Langmuir circulation in the dispersion of surface tracers. *J. Phys. Oceanogr.*, **18**, 1108–1123.

Farmer, D. M., C. L. McNeil, and B. D. Johnson, 1993: Evidence of the importance of bubbles in increasing air–sea gas flux. *Nature,* **361**, 620–623.

Kenney, B. C., 1979: An experimental investigation of the fluctuating currents responsible for the generation of wind rows. Ph.D. thesis, University of Waterloo, 163 pp.

Langmuir, I., 1938: Surface water motion induced by wind. *Science,* **87**, 119–123.

Leibovich, S., 1983: The form and dynamics of Langmuir circulation. *Ann. Rev. Fluid Mech.*, **15**, 391–427.

——, and S. Paolucci, 1981: The instability of the ocean to Langmuir circulations. *J. Fluid Mech.*, **102**, 141–167.

Osborn, T., D. M. Farmer, S. Vagle, S. A. Thorpe, and M. Curé, 1993: Measurements of bubble plumes and turbulence from a submarine. *Atmos.–Ocean,* **30**, 419–440.

Pingree, R. D., and D. K. Griffiths, 1978: Tidal fronts on the shelf seas around the British Isles. *J. Geophys. Res.*, **83**, 4615–4622.

Pollard, R. T., 1977: Observations and theories of Langmuir circulations and their role in near surface mixing. *A Voyage of Discovery; G. Deacon 70th Anniversary Volume,* M. Angel, Ed., Pergamon, 235–251.

Scott, J. C., 1975: The role of salt in whitecap persistance. *Deep-Sea Res.*, **22**, 653–657.

Smith, J. A., 1992: Observed growth of Langmuir circulation. *J. Geophys. Res.*, **97**(C4), 5651–5664.

——, 1993: Performance of a horizontally scanning Doppler sonar near shore. *J. Atmos. Oceanic Technol.*, **10**, 752–763.

Smith, J., R. Pinkel, and R. A. Weller, 1987: Velocity structure in the mixed layer during MILDEX. *J. Phys. Oceanogr.*, **17**, 425–439.

Thorpe, S. A., 1977: Turbulence and mixing in a Scottish loch. *Philos. Trans. Roy. Soc. London A,* **286**, 125–181.

——, 1982: On the clouds of bubbles formed by breaking wind waves in deep water, and their role in air–sea gas transfer. *Philos. Trans. Roy. Soc. London A,* **304**, 155–210.

——, 1984: The effect of Langmuir circulation on the distribution of submerged bubbles caused by breaking wind waves. *J. Fluid Mech.*, **142**, 151–170.

——, 1986: Measurements with an automatically recording inverted echo sounder: ARIES and the bubble clouds. *J. Phys. Oceanogr.*, **16**, 1462–1478.

——, 1988: ". . . Light on obscure oceanographical problems"; an historical review of studies of the physics of Loch Ness. *Scott. Naturalist,* 17–33.

——, 1992: The break-up of Langmuir circulation and the instability of an array of vortices. *J. Phys. Oceanogr.*, **22**, 350–360.

——, 1993: Energy loss by breaking waves. *J. Phys. Oceanogr.*, **23**, 2498–2502.

——, 1994: On the meandering and dispersion of a plume of floating particles caused by the advection of Langmuir circulation in a current. *J. Phys. Oceanogr.*, in press.

——, and P. N. Humphries, 1980: Bubbles and breaking waves. *Nature,* **283**, 463–465.

——, and A. J. Hall, 1982: Observations of the thermal structure of Langmuir circulation. *J. Fluid Mech.*, **114**, 237–250.

——, and ——, 1983: The characteristics of breaking waves, bubble clouds and near-surface currents observed using side-scan sonar. *Contin. Shelf Res.*, **1**, 353–384.

——, and M. Curé, 1994: One dimensional dispersion in a lake inferred from sonar observations. *Mixing and Transport in the*

Environment, Cath Allen Memorial Volume, K. J. Beven, P. C. Chatwin, J. H. Millbank, Eds., Wiley Publications. 17–28.

——, and A. J. Hall, 1994: Near-shore side-scan sonar studies. *J. Atmos. Oceanic Technol.,* **10,** 778–783.

——, M. B. Belloul, and A. J. Hall, 1987: Internal waves and whitecaps. *Nature,* **283,** 463–465.

——, M. Curé, and M. White, 1991: The skewness of temperature derivatives in oceanic boundary layers. *J. Phys. Oceanogr.,* **21,** 428–433.

Wedderburn, E. M., 1907: The temperature of the fresh-water lochs of Scotland, with special reference to Loch Ness. *Trans. Roy. Soc. Edinburgh,* **45,** 407–489.

——, and W. Watson, 1909: Observations with a current meter in Loch Ness. *Proc. Roy. Soc. Edinburgh,* **29,** 619–647.

Weller, R. A., and J. F. Price, 1988: Langmuir circulation within the oceanic mixed layer. *Deep-Sea Res.,* **35,** 711–747.

Woolf, D. K., and S. A. Thorpe, 1991: Bubbles and the air–sea exchange of gases in near-saturation conditions. *J. Mar. Res.,* **49,** 435–466.

Wu, J., 1975: Wind-induced drift currents. *J. Fluid Mech.,* **68,** 47–70.

Zedel, L., and D. M. Farmer, 1991: Organised structures in subsurface bubble clouds: Langmuir circulation in the open ocean. *J. Geophys. Res.,* **96,** 8889–8900.